

Magnetic shear effects on ballooning turbulence in the boundary of fusion devices

Z. Tecchiolli,¹ A. J. Coelho,² J. Loizu,¹ B. De Lucca,¹ and P. Ricci¹

¹*Ecole Polytechnique Fédérale de Lausanne (EPFL), Swiss Plasma Center (SPC), CH-1015 Lausanne, Switzerland*

²*Gauss Fusion GmbH, Garching bei München, Germany*

(*Electronic mail: zeno.tecchiolli@epfl.ch)

(Dated: 8 August 2025)

The effect of magnetic shear on ballooning-driven plasma edge turbulence is studied through nonlinear simulations complemented by linear numerical and analytical investigations. Nonlinear, 3D, global, flux-driven simulations using the GBS code show that the scale separation between radial, x , and poloidal, y , size of turbulent eddies, $k_x \ll k_y$, considered by Ricci, Rogers, and Brunner¹ and extensively used to predict pressure gradient lengths, SOL width, particle and heat fluxes, is observed with high magnetic shear. In contrast, for low magnetic shear, $k_x \sim k_y$ is observed, with fluctuation properties resembling those shown by recent low-shear stellarator simulations reported in Coelho, Loizu, Ricci, and Tecchiolli². Global linear investigations of the ballooning mode qualitatively captures the transition in mode structure with varying magnetic shear, showing that $k_x \ll k_y$ is achieved with sufficiently strong poloidal mode coupling enhanced by increasing magnetic shear, resistivity, toroidal mode number, and equilibrium gradient scale length. This is confirmed by an analytical study considering a dominant poloidal mode and its sidebands, which highlights that the poloidal mode structure is determined by curvature and $k_{||}$ effects.

I. INTRODUCTION

Turbulence in the boundary of tokamaks shows the presence of small-scale eddies originating inside the last closed flux surface (LCFS), that may develop into filaments detaching and propagating into the far scrape-off layer (SOL)^{3,4}. The size of these eddies in the radial and binormal (\sim poloidal) direction is of crucial importance for determining the plasma dynamics in the boundary region⁵⁻⁷.

The eddy size combined with quasi-linear theories⁸ allows for the prediction of fundamental quantities such as the equilibrium pressure gradient length and the SOL width⁹. Indeed, the evaluation of the eddy size is a key element to estimate the particle and heat turbulent fluxes as it affects the turbulent regimes in the boundary^{7,9-11} and the plasma-wall interaction¹². Ultimately, operational limits and turbulent regime transitions such as the density and β operational limits, and of the L-H transition¹³⁻¹⁵ depend on the shape of the turbulent eddies. Scaling laws for the equilibrium lengths and confinement times based on an estimate of the eddy size were successfully validated against multi-machine databases^{14,16-18}.

Previous studies^{1,13,19} have investigated the radial extension of the turbulent eddies in ballooning mode (BM)¹ and drift waves (DWs)¹⁹ driven turbulence. For BM and DWs, the relationship $k_x \sim \sqrt{k_y/L_p}$ is found analytically, where k_x and k_y denote radial and binormal wavenumbers, and L_p is the time-averaged pressure radial scale length. For Kelvin-Helmholtz turbulence^{13,19}, expected to be significant only in the presence of strong $E \times B$ shear flow⁷, the scaling $k_x \sim 0.6k_y$ is observed.

To simplify the study of eddy properties, mode locality assumptions are often made in linear studies of edge instabilities. In the case of ballooning modes (BMs), a key scaling relation, $k_x \sim \sqrt{k_y/L_p}$, is derived by assuming strong

poloidal localization, which holds when $k_y L_p \gg 1$ and a single dominant poloidal mode is considered^{1,19}. The relation $k_x \sim \sqrt{k_y/L_p}$ has been widely used to simplify the eddies analysis, as it ensures $k_x \ll k_y$, allowing radial derivatives of the mode to be neglected. In fact, linear studies often adopt a flux-tube approach^{8,11,19,20}, which assumes $1/L_p \ll k_x, k_y$.

In contrast to tokamak simulations, recent, global, flux-driven, two-fluid, plasma turbulence simulations of an island-diverted stellarator²¹ show a BM dominated regime with $k_x \sim k_y$ eddies and fluctuation scales comparable to equilibrium gradients, $k_y \sim 1/L_p$. Fluctuations with these properties are also found experimentally in the TJ-K stellarator²², a feature successfully reproduced by global turbulent simulations²³. The island diverted configuration and TJ-K both have a small global magnetic shear, $s \equiv (r/q)dq/dr \ll 1$ with r being the radial direction and $q(r)$ the safety factor, while tokamak configurations are characterised by high magnetic shear, $s \sim 2-4$. These recent results motivate a detailed investigation of the size of turbulent eddies as a function of the magnetic shear.

This paper presents low magnetic-shear and a high magnetic-shear simulations of plasma in the edge region of a simple tokamak with circular flux surfaces. Given the high collisionality in the boundary region and being interested in turbulence time scales, the plasma dynamics is described by the drift-reduced Braginskii equations⁸ evolved by GBS, a three-dimensional, global, two-fluid, flux-driven code²⁴. Simulations parameters are chosen to ensure that turbulence is driven by BM, by tuning the ratio between collisionality and mass-ratio¹⁰. Results show that, as magnetic shear decreases, the dominant mode wavenumber k_y decreases, and $k_x \sim \sqrt{k_y/L_p}$ no longer holds. Indeed, the properties of the fluctuations recall those of recent low-shear stellarator simulations, where $k_x \sim k_y$ ^{21,23}. These simulations show that, at low-shear, radial and poloidal fluctuations extend over a region comparable to L_p , breaking the validity of the flux-tube

approximation. Therefore, a global theory is needed to accurately describe the spatial structure of BMs in general magnetic shear conditions, without assuming a fixed relation between L_p and fluctuation size.

We introduce a novel global 3D linear theory demonstrating that, in low-shear regimes, radial and poloidal fluctuations are comparable in size, while $k_x \sim \sqrt{k_y/L_p}$ is recovered in high-shear regimes. The analytical theory supports our numerical results, pointing out that the turbulent mode poloidal structure results from the interplay between magnetic curvature, inducing mode coupling, and parallel gradient effects.

The paper is organized as follows. Section II describes the drift-reduced Braginskii equations used for simulating plasma turbulence in the boundary of fusion devices and the GBS code we use to evolve them. Section III outlines the tokamak configurations with circular flux surfaces and varying magnetic shear considered for our study, and discusses nonlinear results of ballooning-driven turbulence. Section IV details the extended linear ballooning theory in two dimensions, comparing numerical results with a side-band analytical theory. Finally, Section VII provides a discussion of our findings.

II. THE DRIFT-REDUCED BRAGINSKII EQUATIONS

We consider a magnetized plasma modelled by the drift-reduced Braginskii equations, valid at high collisionality under the assumption of perpendicular scale lengths of the dominant modes larger than the ion Larmor radius. This regime often characterizes the plasma boundary of magnetic fusion devices, as well as the core of low-temperature devices such as the TORPEX basic plasma physics experiment²⁵ or the TJ-K stellarator²³. This set of equations is evolved by the GBS code^{26–28}, a three-dimensional, global, two-fluid, flux-driven code that solves the drift-reduced Braginskii equations⁸. GBS evolves all quantities in time, without separation between equilibrium and fluctuating components. In this work, the electrostatic limit of the model is taken, the Boussinesq approximation is employed²⁶ and the gyroviscous terms, as well as the plasma coupling to the neutral dynamics, are neglected, although these are implemented in the most recent version of the GBS code for tokamak simulations²⁷. Within these ap-

proximations, the set of equations considered in this work is

$$\frac{\partial N}{\partial t} = -\frac{\rho_*^{-1}}{B} [\Phi, N] - \nabla_{\parallel} (NV_{\parallel e}) + \frac{2}{B} [C(p_e) - NC(\Phi)] + D_N \nabla_{\perp}^2 N + D_N^{\parallel} \nabla_{\parallel}^2 N + S_n \quad (1)$$

$$\frac{\partial T_e}{\partial t} = -\frac{\rho_*^{-1}}{B} [\Phi, T_e] - V_{\parallel e} \nabla_{\parallel} T_e + \frac{4T_e}{3B} \left[\frac{C(p_e)}{N} + \frac{5}{2} C(T_e) - C(\Phi) \right] + \frac{2T_e}{3N} [0.71 \nabla_{\parallel} j_{\parallel} - N \nabla_{\parallel} V_{\parallel e}] + D_{T_e} \nabla_{\perp}^2 T_e + \chi_{\parallel e} \nabla_{\parallel}^2 T_e + S_{T_e} \quad (2)$$

$$\frac{\partial T_i}{\partial t} = -\frac{\rho_*^{-1}}{B} [\Phi, T_i] - V_{\parallel i} \nabla_{\parallel} T_i + \frac{4T_i}{3B} \left[\frac{C(p_e)}{N} - \frac{5}{2} \tau C(T_i) - C(\Phi) \right] + \frac{2T_i}{3N} [\nabla_{\parallel} j_{\parallel} - N \nabla_{\parallel} V_{\parallel i}] + D_{T_i} \nabla_{\perp}^2 T_i + \chi_{\parallel i} \nabla_{\parallel}^2 T_i + S_{T_i} \quad (3)$$

$$\frac{\partial V_{\parallel e}}{\partial t} = -\frac{\rho_*^{-1}}{B} [\Phi, V_{\parallel e}] - V_{\parallel e} \nabla_{\parallel} V_{\parallel e} + \frac{m_i}{m_e} \left[v j_{\parallel} + \nabla_{\parallel} \Phi - \frac{\nabla_{\parallel} p_e}{N} - 0.71 \nabla_{\parallel} T_e \right] + \eta_{0e} \nabla_{\parallel}^2 V_{\parallel e} + D_{V_{\parallel e}} \nabla_{\perp}^2 V_{\parallel e} \quad (4)$$

$$\frac{\partial V_{\parallel i}}{\partial t} = -\frac{\rho_*^{-1}}{B} [\Phi, V_{\parallel i}] - V_{\parallel i} \nabla_{\parallel} V_{\parallel i} - \frac{1}{N} \nabla_{\parallel} (p_e + \tau p_i) + \eta_{0i} \nabla_{\parallel}^2 V_{\parallel i} + D_{V_{\parallel i}} \nabla_{\perp}^2 V_{\parallel i} \quad (5)$$

$$\frac{\partial \omega}{\partial t} = -\frac{\rho_*^{-1}}{B} [\Phi, \omega] - V_{\parallel i} \nabla_{\parallel} \omega + \frac{B^2}{N} \nabla_{\parallel} j_{\parallel} + \frac{2B}{N} C(p_e + \tau p_i) + D_{\omega} \nabla_{\perp}^2 \omega + D_{\omega}^{\parallel} \nabla_{\parallel}^2 \omega \quad (6)$$

which are closed by

$$\nabla_{\perp}^2 \Phi = \omega - \tau \nabla_{\perp}^2 T_i. \quad (7)$$

In Eqs. (1-7) and in the rest of the paper, the density N , the electron temperature T_e , the ion temperature T_i and the norm of the magnetic field B are normalized to the reference values N_0 , T_{e0} , T_{i0} and B_0 , respectively; electron parallel velocity $V_{\parallel e}$ and ion parallel velocity $V_{\parallel i}$ are both normalized to the sound speed $c_{s0} = \sqrt{T_{e0}/m_i}$; vorticity ω and electrostatic potential Φ are respectively normalized to $T_{e0}/(e\rho_{s0}^2)$ and T_{e0}/e ; time is normalized to R_0/c_{s0} , where R_0 is a reference macroscopic scale length, typically the major radius of the machine; perpendicular and parallel lengths are normalized to the ion sound Larmor radius, $\rho_{s0} = \sqrt{T_{e0}m_i}/(eB_0)$, and R_0 , respectively. The normalized parallel current density is $j_{\parallel} = N(V_{\parallel i} - V_{\parallel e})$.

The dimensionless parameters appearing in Eqs. (1-7) are the normalized ion sound Larmor radius $\rho_* = \rho_{s0}/R_0$, the normalized electron and ion parallel heat diffusivities, $\chi_{\parallel e}$ and $\chi_{\parallel i}$, considered constant here, the ion to electron temperature ratio $\tau = T_{i0}/T_{e0}$, the normalized electron and ion viscosities, η_{0e} and η_{0i} , which we assume to have constant values, and the

Top/Bottom walls		Inner/Outer walls
$V_{ e}$	$V_{ e} = \pm \sqrt{T_e} \exp(\Lambda - \Phi/T_e)$	$\partial_s V_{ e} = 0$
$V_{ i}$	$V_{ i} = \pm \sqrt{T_e} F_T$	$\partial_s V_{ i} = 0$
ω	$\omega = - \left[\frac{(\partial_s v_{ i})^2}{F_T^2} \pm \frac{\sqrt{T_e}}{F_T} \partial_s^2 v_{ i} \right]$	$\omega = 0$
n	$\partial_s n = \mp \frac{n}{\sqrt{T_e} F_T}$	$\partial_s n = 0$
Φ	$\partial_s \Phi = \pm \frac{\sqrt{T_e}}{F_T} \partial_s v_{ i} / \Phi = \Lambda T_e$	$\Phi = \Lambda T_e$
T_e, T_i	$\partial_s T_e = \partial_s T_i = 0$	$\partial_s T_e = \partial_s T_i = 0$

TABLE I. Boundary conditions for the simulations presented in this paper. The derivative $\partial_s = \mathbf{s} \cdot \nabla$ is along the direction normal to the surface.

normalized Spitzer resistivity, $\nu = \nu_0 T_e^{-3/2}$, with

$$\nu_0 = \frac{4\sqrt{2}\pi}{5.88} \frac{e^4}{(4\pi\epsilon_0)^2} \frac{\sqrt{m_e} R_0 N_0 \lambda}{m_i c_{s0} T_{e0}^{3/2}}, \quad (8)$$

where λ denotes the Coulomb logarithm⁷. Small numerical diffusion terms such as $D_N \nabla_\perp^2 N$ and $D_N^\parallel \nabla_\parallel^2 N$ (and similar for the other fields) are introduced to improve the numerical stability of the simulations. The simulation results show that they have a negligible effect the plasma dynamics since they lead to significantly lower perpendicular transport than the turbulent phenomena. The terms S_N , S_{T_e} and S_{T_i} denote the density, electron temperature and ion temperature sources, respectively. Magnetic pre-sheath boundary conditions Loizu *et al.*²⁹, Masetto *et al.*³⁰ are applied to all quantities on the domain boundaries where the plasma is exhausted (the top and bottom domain boundaries in this work). A summary of the applied boundary conditions is given in Table I.

Considering a generic scalar quantity f , the normalized geometrical operators appearing in Eqs. (1-7) are the parallel gradient $\nabla_\parallel f = \mathbf{b} \cdot \nabla f$, the Poisson brackets, $[\Phi, f] = \mathbf{b} \cdot [\nabla \Phi \times \nabla f]$, the curvature operator, $C(f) = (B/2) [\nabla \times (\mathbf{b}/B)] \cdot \nabla f$, the parallel Laplacian, $\nabla_\parallel^2 f = \mathbf{b} \cdot \nabla (\mathbf{b} \cdot \nabla f)$, and the perpendicular Laplacian $\nabla_\perp^2 f = \nabla \cdot [(\mathbf{b} \times \nabla f) \times \mathbf{b}]$. By assuming $B_p/B \ll 1$, where B_p is the poloidal magnetic field, and $l_\perp/l_\parallel \ll 1$, where l_\perp and l_\parallel are the perpendicular and parallel turbulence length scales, and only retaining the leading order terms, the geometrical operators in an axisymmetric field in cylindrical coordinates (R, φ, Z) become²⁷:

$$\nabla_\parallel f = \frac{B_R}{B} \rho_*^{-1} \frac{\partial f}{\partial R} + \text{sign} \left(\frac{B_\varphi}{B} \right) \frac{R_0}{R} \frac{\partial f}{\partial \varphi} + \frac{B_Z}{B} \rho_*^{-1} \frac{\partial f}{\partial Z} \quad (9)$$

$$[\Phi, f] = \text{sign} \left(\frac{B_\varphi}{B} \right) \left[\frac{\partial \Phi}{\partial Z} \frac{\partial f}{\partial R} - \text{sign} \left(\frac{B_\varphi}{B} \right) \frac{\partial \Phi}{\partial R} \frac{\partial f}{\partial Z} \right] \quad (10)$$

$$C(f) = \text{sign} \left(\frac{B_\varphi}{B} \right) \frac{\partial f}{\partial Z} \quad (11)$$

$$\nabla_\perp^2 f = \frac{\partial^2 f}{\partial R^2} + \frac{\partial^2 f}{\partial Z^2} \quad (12)$$

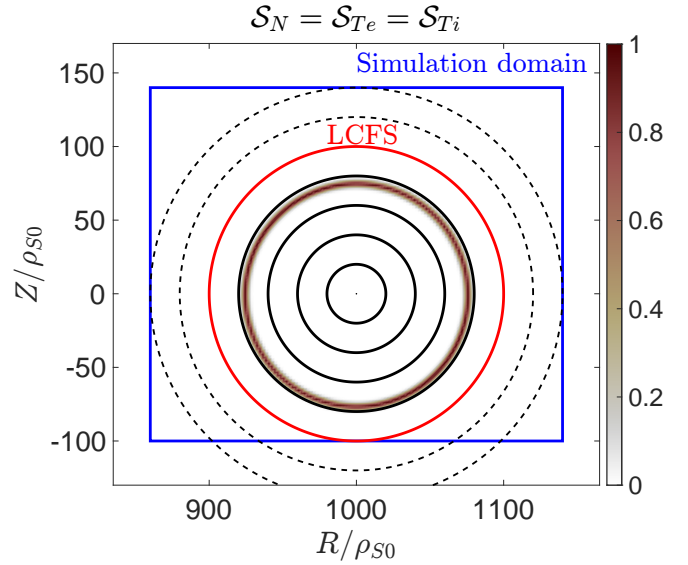


FIG. 1. Poincaré plot of the tokamak magnetic field Eqs. (13-15). The GBS simulation domain is shown in blue. Closed flux surfaces are represented by continuous lines and open flux surfaces by dashed black lines. These are separated by the LCFS in red. The colorscale is for density, electron temperature and ion temperature sources.

The parallel gradient is normalised to $1/R_0$, the perpendicular Laplacian to $1/R_0^2$, the Poisson brackets to $1/\rho_{s0}^2$, and the curvature to $1/R_0 \rho_{s0}$. The GBS simulation domain is a torus of radius R_0 with a rectangular cross-section of size $L_R \times L_Z$.

The physical model in Eqs. (1-7) is discretized using a regular cylindrical grid. Equations (1-6) are advanced in time using an explicit Runge-Kutta fourth-order scheme, while spatial derivatives are computed with a fourth-order finite difference scheme.

III. SIMULATIONS SETUP AND NONLINEAR RESULTS

In the present work, our simulations consider an axisymmetric vacuum magnetic field with circular flux surfaces, assuming a toroidal current density, J , centred around (R_0, Z_0) , and described by a Gaussian profile, $J \sim e^{-r^2/w^2}$, with r the poloidal distance from (R_0, Z_0) and w a constant. This results in a magnetic field whose components in cylindrical coordinates are given by

$$B_R = B_0 \varsigma \frac{Z - Z_0}{(R - R_0)^2 + (Z - Z_0)^2} h(R, Z), \quad (13)$$

$$B_\varphi = B_0 R_0 / R, \quad (14)$$

$$B_Z = -B_0 \varsigma \frac{R - R_0}{(R - R_0)^2 + (Z - Z_0)^2} h(R, Z), \quad (15)$$

with $h(R, Z) = 1 - \exp \{ - [(R - R_0)^2 + (Z - Z_0)^2 / w^2] \}$, B_0 the magnetic field on axis, and ς is constant representing the typical length scale for the poloidal field. The magnetic field in Eqs. (13-15) generates circular flux surfaces (as shown Fig. 1) and corresponds to the one considered in the $s - \alpha$ ge-

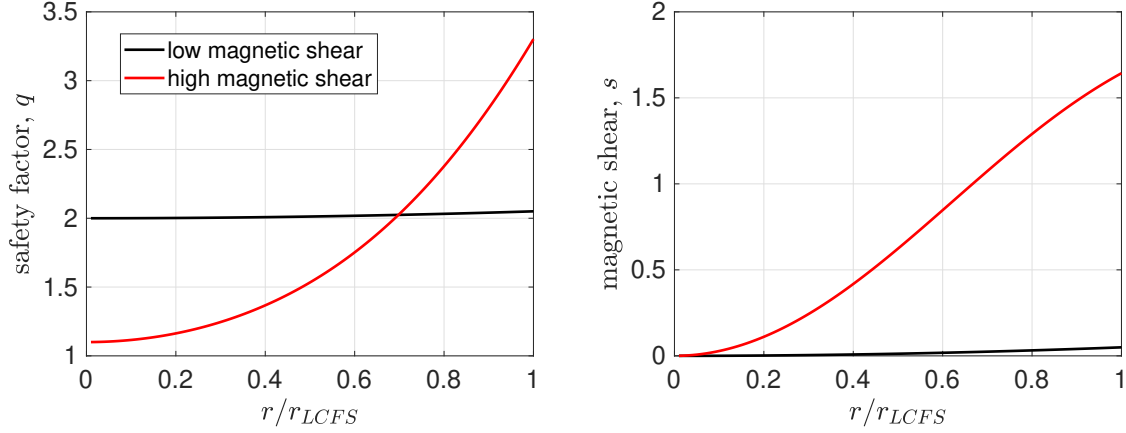


FIG. 2. Safety factor and magnetic shear of the two circular tokamak configurations. In the low magnetic-shear case $s_a = 0.05$, while in the high shear case $s_a = 1.6$.

ometry with $\alpha = 0^{31}$, since we do not include any Shafranov shift and electromagnetic effects. Previous two-fluid turbulence simulations in stellarators^{23,24} also considered electrostatic turbulence on a fixed vacuum field. This configuration was previously employed for studies of the SOL instabilities and turbulent regimes in limited plasmas^{6,10,20}, showing no instability threshold for the resistive BM.

The parameters φ and w are adjusted to fix the values of the safety factor q at the magnetic axis and at the LCFS ($r = a$). In fact, since $B^\theta = B_R \sin \theta / r - B_Z \cos \theta / r$ and $B^\varphi = B_\varphi / R$, and considering that flux surfaces are circular, the safety factor follows as

$$q(r) = \frac{1}{2\pi} \int_0^{2\pi} \frac{B^\varphi}{B^\theta} d\theta = \frac{1}{R_0 \varphi} \frac{r^2}{1 - \exp(-r^2/w^2)} \quad (16)$$

in the infinite aspect-ratio limit,

where (r, φ, θ) are the right-handed toroidal coordinates. Thus, the safety factor on axis is $q_0 = w^2/(R_0 \varphi)$, which allows us to write $w^2 = R_0 \varphi q_0$. The value of q at the LCFS, $q(r = a) = q_a$, allows us to obtain the parameter φ by solving Eq. (16) in the large aspect ratio. The magnetic shear, $s = (r/q)dq/dr$, yields

$$s(r) = 2 + \frac{2r^2}{R_0 \varphi q_0 \left[1 - \exp\left(-\frac{r^2}{R_0 \varphi q_0}\right) \right]}. \quad (17)$$

We note that $s(r = 0) = 0$ and $s(r \rightarrow \infty) = 2$, i.e. the magnetic shear is bounded by 2 in the equilibria considered here.

For our investigations, we consider two configurations: a low magnetic-shear with $q_0 = 2$ and $q_a = 2.05$, and a high magnetic-shear with $q_0 = 1.1$ and $q_a = 3.3$. By setting $R_0 = 1000\rho_{s0}$ and $a = 100\rho_{s0}$, this requires $\varphi = 100\rho_{s0}$ and $w = 447\rho_{s0}$ in the low magnetic-shear case, while $\varphi = 3.22\rho_{s0}$ and $w = 59.3\rho_{s0}$ in the high magnetic-shear case. The safety factor and magnetic shear profiles for the two configurations are shown in Fig. 2. The values of magnetic shear at the LCFS in the two configurations are $s_a = 0.05$ and $s_a = 1.6$. The high shear value is in line with typical edge shear values

for tokamak discharges, $s \approx 1.0 - 4.0$, such as in the case of TCV³²⁻³⁴. While fusion-relevant tokamaks operate with large magnetic shear at the edge, basic plasma studies can be performed in tokamaks with low-shear profiles. This is the case of the Madison Symmetric Torus (MST) operated in a tokamak configuration³⁵, able to nondisruptively operate³⁶ with q -value at the edge between $0.8 - 2$ while q on the axis is 1 with low normalised $\beta < 1\%$. Nevertheless, owing to its thick, stabilizing, conductive wall, MST reached tokamak plasmas with density up to 10 times the Greenwald limit³⁷ with low q at the edge.

The GBS simulation parameters considered here are $\rho_*^{-1} = 1000$, $v_0 = 0.1$, $m_i/m_e = 200$, $\tau = 1$, $\chi_{\parallel e,i} = \eta_{0e,i} = 1.0$, $D_N = D_{Te} = D_{Ti} = D_{V\parallel e} = D_{V\parallel i} = D_\omega = 10$, $D_N^\parallel = D_\omega^\parallel = 1$, a grid resolution of $\Delta R = \Delta Z = 2\rho_{s0}$, $\Delta\phi = 2\pi/80$, and a time-step of the order of $2.0 \times 10^{-5} R_0/c_{s0}$. The density and temperature sources are equal and correspond to a radially localized Gaussian around a closed flux surface near the LCFS, as shown in Fig. 1. Starting from an initial state with constant profiles, a quasi-steady state is reached after a transient where sources, parallel and perpendicular transport, and losses at the walls balance each other. To ensure statistically meaningful results, we time average quantities within a window of 20 time units during the steady state. Time average quantities are indicated with $\langle f \rangle_t$, and time fluctuations are defined as $\tilde{f} \equiv f - \langle f \rangle_t$.

As shown in Fig. 3, the high-shear configuration shows higher peak pressure values in the core region than the low-shear configuration, leading to high energy confinement time $\tau_E = \int \langle p_e + \tau p_i \rangle_t dV / \int S_p dV$, since the power source S_p is the same in the two configurations. On the other hand, $L_p \sim -p/\nabla p$ are comparable close to the LCFS, with $L_p = 20.3$ in the low-shear case and $L_p = 24.1$ in the high-shear case.

A typical snapshot of density and potential fluctuations, \tilde{N} and $\tilde{\Phi}$, of the low and high shear tokamak configurations are shown in Fig. 4. The low magnetic-shear simulation shows larger structures, in particular for the electrostatic potential, than in the high shear simulation.

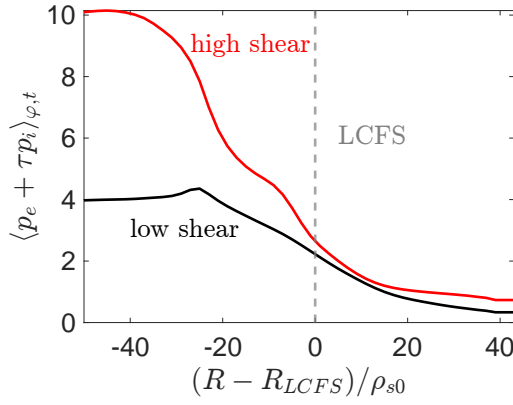


FIG. 3. Toroidally and time-averaged pressure profiles $\langle p_e + \tau p_i \rangle_{\varphi,t}$ close to the LCFS at $Z = 0$ for the high-shear (red) and low-shear (black) cases.

The poloidal and toroidal spectra of fluctuations on a flux surface close to the LCFS are shown in Fig. 5 for the low and high magnetic-shear simulations. The dominant modes are such that $n/m = 1/2$ (in the low-shear simulation) and $n/m = 3/8$ (in the high-shear simulation). These values correspond to $1/q$ around the steepest part of the equilibrium pressure, implying that $k_{\parallel} = (B^{\phi}/B)(m/q - n)$ of the dominant mode approximately vanishes in both simulations, and thus modes are field-aligned. Moreover, the average phase shift between density and potential fluctuations is around $\pi/2$ with $\tilde{\Phi} \gg \tilde{N}$ and the density and $E \times B$ fluctuations show large amplitude on the low-field side. These features suggest that turbulence originates from curvature-driven instabilities, such as BMs. This is also verified by tests where we zero out the interchange drive, i.e. the curvature term in Eq. (6), $C(pe + \tau pi)$, and we observe a significant steepening of the pressure profile. Indeed, previous studies of SOL turbulent regimes in limited tokamaks¹⁰ predict that turbulence is driven by resistive BMs at the considered values of v_0 and s for both values of shear.

The value of $k_y \rho_{s0}$ of the dominant mode, which is proportional to m , is significantly larger in the high-shear case, as Fig. 5 shows, with $m = 8$ in the high-shear simulation and $m = 2$ in the low-shear case. In the low-shear results, we observe that the poloidal extension of the structures is of the order of the radial extension and of L_p , which is comparable to a , i.e. $k_y \sim k_x \sim 1/L_p$, and the relation $k_x \ll k_y$ does not apply.

We further note that a larger number of modes are excited in the high-shear case than in the low-shear. To explain this, we note that the growth rate of BM peaks at $k_{\parallel} \approx 0$, implying $m/n \sim q$. In the low-shear case, since $q(r) \approx q_0$ with q_0 for all r , only one combination of (m, n) , up to a common multiplicative factor for m and n providing the same m/n , makes k_{\parallel} minimal. On the other hand, in the high-shear case, a larger number of combinations of m/n minimise k_{\parallel} given that q is a function of the radial position and thus crosses several rational numbers. Therefore, a large number of modes, possibly developing into broad-band turbulence, are expected to be present in a high-shear configuration. Indeed, the simulation results show that fluctuations in the low shear case are coherent, with

the dominant $m = nq_0$ mode across the radial profile; while in the high-shear case the dominant m and n vary across the radial profile to satisfy the field-aligned property. Among the possible combinations of m/n , the simulation usually presents the lowest possible m value, which leads to larger transport at this scales typically with m^{-2} as shown in Zeiler⁸.

Similar results to the high-shear case have been obtained with $q_0 = 1$ and $q_a = 4$, and with $q_0 = 2$ and $q_a = 4$ (data not shown). We remark that the turbulent modes are coherent in the low-shear regime for larger safety factor values. Indeed, simulations with $q_0 = 4$ and $q_a = 4.1$ reveal that the potential presents a large and radially elongated mode with $m = 4$ (see in Fig. 6). In addition, when a flat q -profile is considered, also with a highly irrational value of flat q , namely the golden ratio $q_0 = (1 + \sqrt{5})/2 \simeq 1.61$ (the hardest irrational number approximated by fractions), we observe radially and poloidally elongated structures with higher dominant mode numbers at $m/n = 13/8 \approx q_0$ (simulation results not shown). In this case, the fluctuation spectrum still shows coherent features, similar to those in Figure 5 a), approximately independent of the radial profile. These results demonstrate that a low magnetic shear significantly influences the properties of tokamak edge turbulence, providing a new regime with coherent features such that $k_x \sim k_y \sim 1/L_p$, which has not been reported by previous simulations.

We remark that in Giacomini and Ricci¹⁵, a regime where $1/k_x \sim L_p$ has been related to pressure profile collapse and the crossing of the density limit. However, our simulations consider values of v_0 and density that are far away from this limit. Moreover, $k_y \ll k_x$ was still considered in the analysis of the degraded confinement regime studied by Giacomini and Ricci¹⁵. Finally, we note that in the MST employed as a tokamak, characterised by a low-shear, low- β configuration, interchange-like modes are also indicated as possible instabilities^{36,37}. More recently, large "snake structures" dominating the dynamics with $m = n = 1$ have been observed in MST³⁸ for q at the edge larger than 2.2 with q at the axis 1.

IV. GLOBAL LINEAR THEORY FOR BALLOONING MODES

We now show that the differences between low shear and high shear can be explained using a linear model. Since turbulence is driven by ballooning instabilities in the simulations presented here, we consider a reduced model from Eqs. (1-7) that includes the main elements of the ballooning instability^{11,20}. First, we consider the cold ion limit, $T_i = 0$, and we neglect sound waves, assuming $k_{\parallel} \ll \partial_t$ (or $c_{s0}k_{\parallel} \ll \partial_t$ in physical units). We also neglect drift waves, with the hypothesis $\omega_{de} \ll \partial_t$, where $\omega_{de} = \mathbf{k} \cdot \mathbf{V}_{de}$ is the diamagnetic frequency, and $\mathbf{V}_{de} = \nabla T_e \times \mathbf{b}/(eNB)$ is the diamagnetic velocity. Finally, we neglect compressibility terms associated with the curvature effects in the density and temperature equations. As a result, the electrons and ions dynamics are decoupled, and, focusing on the electrons species (subscripts are dropped in

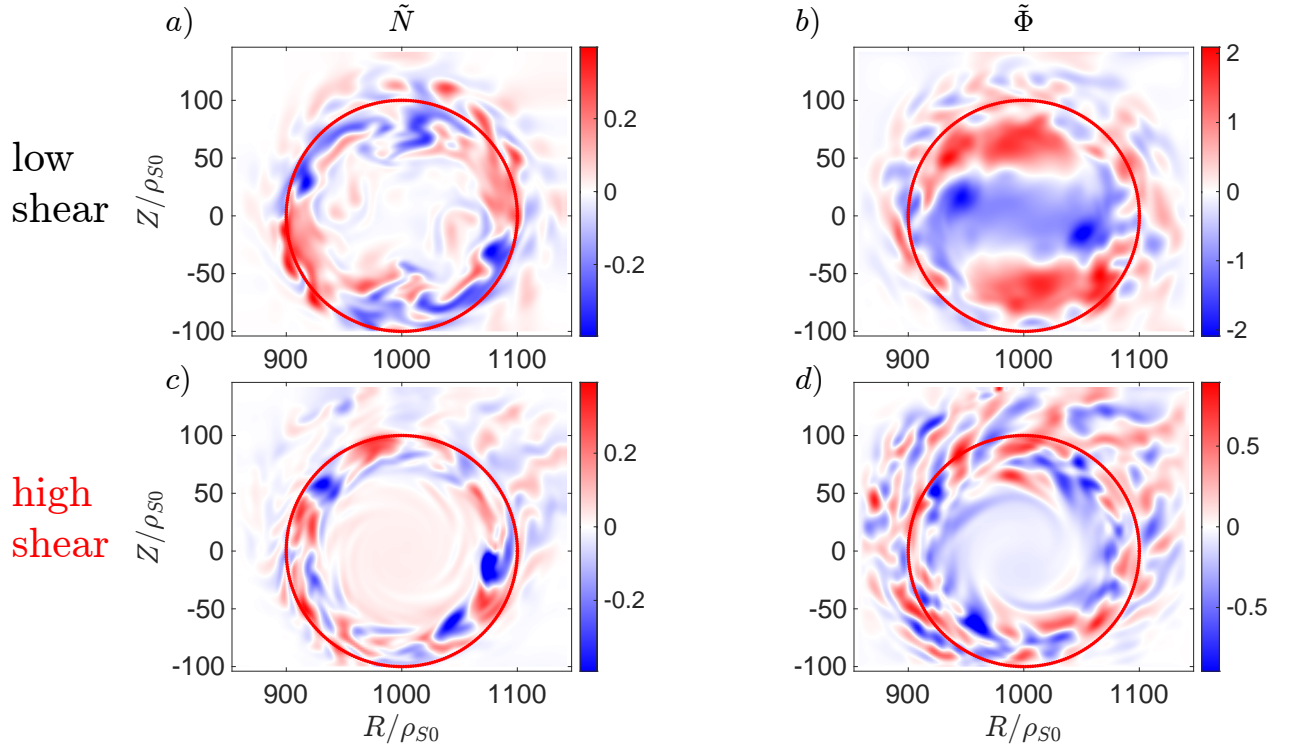


FIG. 4. Typical density and potential fluctuations of low ($s_a = 0.05$) and high ($s_a = 1.6$) magnetic shear tokamak configurations.

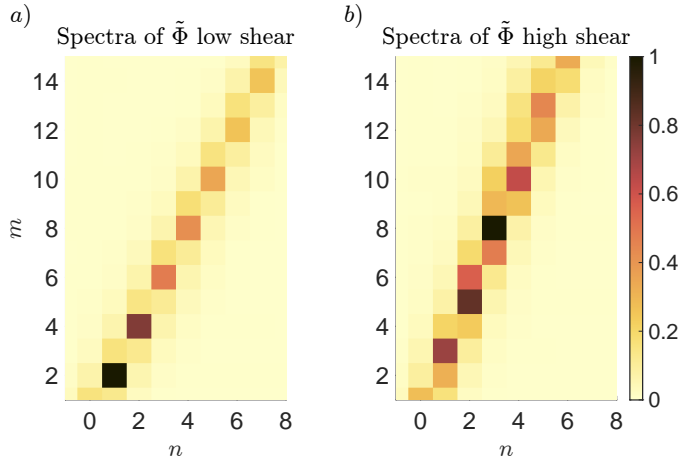


FIG. 5. Time-averaged Fourier spectrum of potential fluctuations on the LCFS in the two tokamak configurations with low, $s_a = 0.05$ in (a), and high, $s_a = 1.6$ in (b), magnetic shear.

the following for clarity), we consider:

$$\frac{\partial N}{\partial t} = -\frac{\rho_*^{-1}}{B} [\Phi, N], \quad (18)$$

$$\frac{\partial T}{\partial t} = -\frac{\rho_*^{-1}}{B} [\Phi, T], \quad (19)$$

$$\frac{\partial V}{\partial t} = -v \left(\frac{m_i}{m_e} \right) NV + \left(\frac{m_i}{m_e} \right) \nabla_{\parallel} \Phi, \quad (20)$$

$$\frac{\partial \nabla_{\perp}^2 \Phi}{\partial t} = -\frac{\rho_*^{-1}}{B} [\Phi, \nabla_{\perp}^2 \Phi] - \frac{B^2}{N} \nabla_{\parallel} (NV) + \frac{2B}{N} C(NT). \quad (21)$$

The BM drive is given by the curvature-driven term $C(NT)$ in Eq. (21). In the (r, φ, θ) coordinate system and expanding in the large aspect ratio, the normalised geometrical operators in Eqs. (9-12) become:

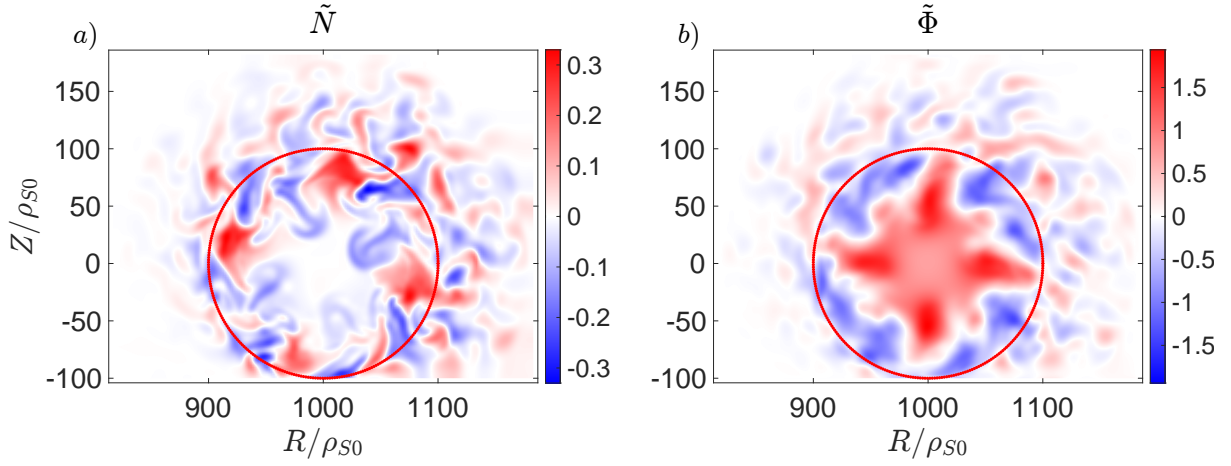
$$\nabla_{\parallel} f = \frac{1}{q} \frac{\partial f}{\partial \theta} + \frac{\partial f}{\partial \varphi}, \quad (22)$$

$$[\Phi, f] = \frac{1}{r} \left(\frac{\partial \Phi}{\partial r} \frac{\partial f}{\partial \theta} - \frac{\partial \Phi}{\partial \theta} \frac{\partial f}{\partial r} \right) \quad (23)$$

$$C(f) = \sin \theta \frac{\partial f}{\partial r} + \frac{\cos \theta}{r} \frac{\partial f}{\partial \theta} \quad (24)$$

$$\nabla_{\perp}^2 f = \frac{\partial^2 f}{\partial r^2} + \frac{1}{r} \frac{\partial f}{\partial r} + \frac{1}{r^2} \frac{\partial^2 f}{\partial \theta^2}. \quad (25)$$

We linearise Eqs. (18- 21) by expressing a field f as $f(t, r, \theta, \varphi) = f_0(r) + \tilde{f}(t, r, \theta, \varphi)$ with $\tilde{f} = \sum_n e^{\sigma n t} e^{-i n \varphi} f_n(r, \theta)$, where f_0 is the equilibrium

FIG. 6. Density and potential fluctuations at low shear when $q_0 = 4$ and $q_a = 4.1$.

background, $\tilde{f} \ll f_0$ its perturbation, $\sigma_n = \gamma_n + i\omega_n$ with γ_n the growth rate and ω_n the real frequency, and the perturbation \tilde{f} is decomposed toroidally into Fourier modes, with n the toroidal mode number. For simplicity, we drop the subscript n from f , γ and ω in the following. We set $\Phi_0 = 0$ which is equivalent to analyse the mode evolution in the reference frame rotating poloidally with the $E \times B$ drift. We neglect parallel velocity shear effects imposing $V_0 = 0$. Moreover, we assume $n_0 = T_0 = f_0(r)$, with f_0 given by

$$f_0(r) = \frac{1}{h} \log \left[\tanh\left(\frac{\alpha - r}{L_0}\right) + f_{00} \right], \quad (26)$$

where

$$\alpha = \hat{r} + \frac{L_0}{4} \log \frac{f_{00} - 1}{f_{00} + 1}, \quad (27)$$

having defined

$$h = \log \left[f_{00} + \tanh \left(\frac{\hat{r}}{L_0} + \frac{1}{4} \log \frac{f_{00} - 1}{f_{00} + 1} \right) \right], \quad (28)$$

We remark that f'_0 peaks at $r = \hat{r}$, the parameter L_0 controls the characteristic gradient length scale of f_0 , and the constant f_{00} is a dimensionless parameter that sets the background value. In the present analysis we consider different values of L_0 , from $L_0/a = 0.03$ corresponding to a localised, large equilibrium gradient, to $L_0/a = 0.3$ corresponding to a distributed, small equilibrium gradient. We take $\hat{r} = a/2$, to center the profile in the radial direction, and $f_{00} = 2$, and we refer to the values of magnetic shear and safety factor at \hat{r} as \hat{s} and \hat{q} , respectively. We center the equilibrium profile in the domain to improve smoothness at $r = 0$ and $r = a$.

With these hypotheses, we linearise Eqs. (18-21) with the

geometrical operators given in Eqs. (22-25), yielding

$$\sigma N = \sigma T = \left[-\rho_*^{-1} \frac{f'_0}{r} \frac{\partial}{\partial \theta} \right] \Phi, \quad (29)$$

$$\sigma V = \left[-\frac{m_i}{m_e} v_0 \frac{1}{f_0^{1/2}} \right] V + \frac{m_i}{m_e} \left[\frac{1}{q} \frac{\partial}{\partial \theta} - in \right] \Phi, \quad (30)$$

$$\begin{aligned} \sigma \left[\frac{\partial^2}{\partial r^2} + \frac{1}{r} \frac{\partial}{\partial r} + \frac{1}{r^2} \frac{\partial^2}{\partial \theta^2} \right] \Phi = & \left[-2 \frac{\sin \theta}{f_0} f'_0 + 2 \sin \theta \frac{\partial}{\partial r} \right. \\ & + 2 \frac{\cos \theta}{r} \frac{\partial}{\partial \theta} \left. \right] N + \left[2 \frac{\sin \theta}{f_0} f'_0 + 2 \sin \theta \frac{\partial}{\partial r} + 2 \frac{\cos \theta}{r} \frac{\partial}{\partial \theta} \right] T \\ & - \left[\frac{1}{q} \frac{\partial}{\partial \theta} - in \right] V, \end{aligned} \quad (31)$$

where the prime stands for the radial derivative.

In the following, we exploit the field-aligned nature of the ballooning mode²⁰ to simplify the eigenvalue problem in Eqs. (29-31). Since $k_{\parallel} \sim m/q - n$, the radial profile of q has an impact on the field-aligned structure of the mode. Hence, we consider separately a constant and a varying q along r , i.e. vanishing and non-vanishing profiles of magnetic shear, respectively.

We first consider the non-vanishing shear case. We use the ballooning transform^{39,40}, expressing a toroidal mode $\tilde{f}(r, \theta)$ as:

$$\tilde{f}(r, \theta) = \sum_{m=-\infty}^{+\infty} e^{-im\theta} \int_{-\infty}^{+\infty} e^{im\eta} \hat{f}(r, \eta) d\eta, \quad (32)$$

by performing a transformation from the periodic coordinate $\theta \in [0, 2\pi)$ to $\eta \in (-\infty, +\infty)$. As showed in⁴¹, the transformation in Eq. (32) preserves the spectrum of the eigenvalue problem in Eqs. (29-31) assuming that \hat{f} vanishes for $\eta \rightarrow \pm\infty$. By construction, \hat{f} is not periodic and, therefore, each field can be expressed in an eikonal form

$$\hat{f}(r, \eta) = u_f(r, \eta) e^{iS}, \quad (33)$$

where S is the fast-varying eikonal function, and u_f is the slowly oscillating envelope, so that $\nabla_{\parallel} S = 0$. In our case, considering the toroidal phase component of the mode, the eikonal function is $S = n[\varphi + q(r)\eta + \eta_0]$. The value η_0 represents the poloidal angle where the perturbation has a local maximum amplitude, being a free parameter of the problem. Given the poloidal symmetry of Eqs. (29-31), this is either $\eta_0 = 0$ or $\eta_0 = \pi$. A numerical investigation on the influence of η_0 on γ shows that the growth rate is maximum for $\eta_0 = 0$, consistently with the ballooning instability peaking at the low field side. Hence, we take $\eta_0 = 0$ in the following.

The reconstruction of the mode is then performed according to Taylor and Newton⁴², that is

$$\tilde{f}(r, \theta) = \sum_M e^{-inq(\theta - 2\pi M)} u_f(r, \theta - 2\pi M), \quad (34)$$

Expressing N , T , V and Φ with the ballooning transformation in Eq. (32) in the eigenvalue problem in Eqs. (29-31), and employing the eikonal form in Eq. (33), we obtain:

$$\sigma N = \sigma T = \left[-\rho_*^{-1} \frac{f'_0}{r} \left(\frac{\partial}{\partial \eta} - inq \right) \right] \Phi \quad (35)$$

$$\sigma V = \left[-\frac{m_i}{m_e} v_0 \frac{1}{f_0^{1/2}} \right] V + \frac{m_i}{m_e} \left[\frac{1}{q} \frac{\partial}{\partial \eta} \right] \Phi \quad (36)$$

$$\begin{aligned} \sigma \left[\frac{\partial^2}{\partial r^2} + \frac{1}{r} \frac{\partial}{\partial r} + \frac{1}{r^2} \frac{\partial^2}{\partial \eta^2} - 2in\eta q' \frac{\partial}{\partial r} - 2in \frac{q}{r^2} \frac{\partial}{\partial \eta} - in \frac{q'}{r} \eta \right. \\ \left. - n^2 \eta^2 (q')^2 - in\eta q'' - n^2 \frac{q^2}{r^2} \right] \Phi \\ = 2 \left[-\frac{\sin \eta}{f_0} f'_0 + \sin \eta \frac{\partial}{\partial r} + \frac{\cos \eta}{r} \frac{\partial}{\partial \eta} - in \sin \eta q' \eta - in \frac{\cos \eta}{r} q \right] T \\ + 2 \left[\frac{\sin \eta}{f_0} f'_0 + \sin \eta \frac{\partial}{\partial r} + \frac{\cos \eta}{r} \frac{\partial}{\partial \eta} - in \sin \eta q' \eta - in \frac{\cos \eta}{r} q \right] T \\ - \left[\frac{1}{q} \frac{\partial}{\partial \eta} \right] V. \end{aligned} \quad (37)$$

To simplify the notation, in Eqs. (35-37) we denote the envelope of the eikonal part of the ballooning representation, u_f in Eq. (33), simply with the corresponding field f , i.e. indicate u_f with f . We remark that, in this work, the ballooning representation is not used for decoupling parallel and perpendicular dynamics by taking the ideal ballooning limit of $n \rightarrow \infty$, as it is classically done in magnetohydrodynamics (MHD)³⁹. Here, we only use the ballooning transform as a representation, similarly to the approach used in PEST-II⁴³.

In the limit of low shear and low n , the ballooning representation breaks down due to the fact that the solutions u , and \hat{f} , are not localised in η . This problem is well known in MHD where the criterion of the validity of such representation is $n \gg (\psi q')^{-2}$, where ψ is the poloidal magnetic flux, making the vanishing shear case pathological⁴⁴. Even though the identification of a similar criterion for Eqs. (18-21) goes beyond the scope of this work, an initial numerical investigation

suggests that the representation in Eq. (32) is not suited for investigations in the low-shear regime considered in this paper.

For the low-shear cases we proceed as explained in Hastie and Taylor⁴⁴. We consider the following representation for the fields in Eqs. (29-31):

$$\tilde{f}(r, \theta, \phi) = \hat{f}(r, \theta) e^{i(m\theta - n\phi)}, \quad (38)$$

where $m = nq_0$. Using the representation in Eq. (38) into the eigenvalue problem in Eqs. (29-31), we obtain:

$$\sigma N = \sigma T = \left[-\rho_*^{-1} \frac{f'_0}{r} \left(\frac{\partial}{\partial \theta} - im \right) \right] \Phi, \quad (39)$$

$$\sigma V = \left[-\frac{m_i}{m_e} v_0 \frac{1}{f_0^{1/2}} \right] V + \frac{m_i}{m_e} \left[\frac{1}{q} \frac{\partial}{\partial \theta} \right] \Phi, \quad (40)$$

$$\begin{aligned} \sigma \left[\frac{\partial^2}{\partial r^2} + \frac{1}{r} \frac{\partial}{\partial r} - \frac{m^2}{r^2} \right] \Phi = \left[-2 \frac{\sin \theta}{f_0} f'_0 + 2 \sin \theta \frac{\partial}{\partial r} \right. \\ \left. + 2 \frac{\cos \theta}{r} \left(\frac{\partial}{\partial \theta} - im \right) \right] N \left[2 \frac{\sin \theta}{f_0} f'_0 + 2 \sin \theta \frac{\partial}{\partial r} \right. \\ \left. + \frac{\cos \theta}{r} \left(\frac{\partial}{\partial \theta} - im \right) \right] T - i \left[\frac{1}{q} \frac{\partial}{\partial \theta} \right] V. \end{aligned} \quad (41)$$

To simplify the notation also in this case, we drop the hat, which is present in Eq. (38), in Eqs (39-41). The two representations in Eqs.(38) and (32) allow solving the dynamics without fast oscillating modes in the poloidal plane, using lower resolution and, thus, accelerating numerical convergence.

A numerical implementation of the three eigenvalue problems, Eqs. (29-31), (35-37) and Eqs. (39-41), is based on a finite difference scheme with an iterative solver that makes use of a Krylov-Schur algorithm for large sparse eigenvalue problems⁴⁵ implemented by `eigs` function of MATLAB⁴⁶. Details are reported in Appendix A. In our analysis, we consider the eigenvalue (and their corresponding eigenvectors) with the largest growth rate.

The eigenvalue and eigenmodes computed via the low-shear representation in Eq. (38) and via the ballooning representation in Eq. (32) for high-shear cases are successfully verified by benchmarking these with the direct solution of Eqs. (29-31) in fully converged cases for $n \lesssim 12$, showing that these representations correctly capture the BM dynamics in the corresponding shear regimes. Therefore, if not specified otherwise, in the following we compute vanishing shear results solving Eqs. (39-41), and for non-vanishing shear cases, we solve Eqs. (35-37). The results in the following sections are obtained by fixing the value of $q_0 = 2$ and increasing q_a , effectively increasing the local values of q and s at the peak of the equilibrium gradient. If not specified otherwise, we fix $m_i/m_e = 200$, $v_0 = 0.1$, $\rho_*^{-1} = 1000$, $a = 100\rho_{s0}$, and $L_0 = 0.2a$.

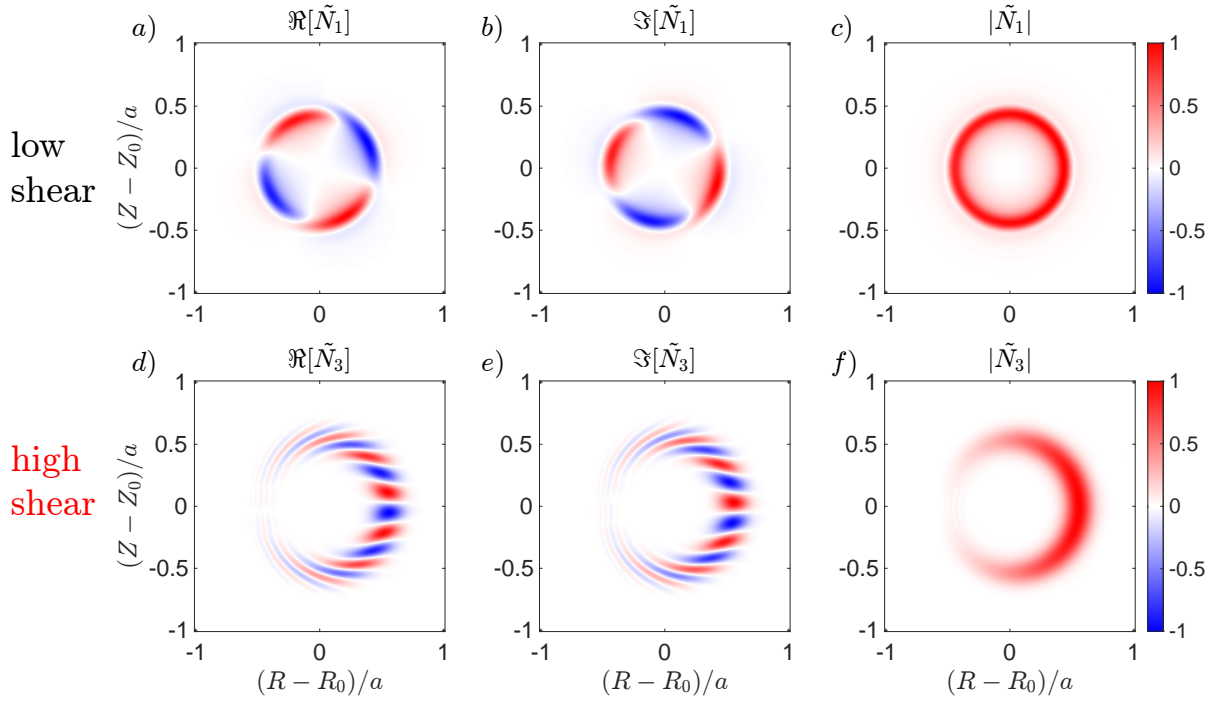


FIG. 7. Radial-poloidal mode structure for fastest growing BM in the low shear case ($\hat{s} = 0, \hat{q} = 2.0$) with $n = 1$ (top) and in the high shear ($\hat{s} = 1.6, \hat{q} = 2.0$) with $n = 3$ (bottom). Real (left), imaginary (middle) parts and module (right) are considered.

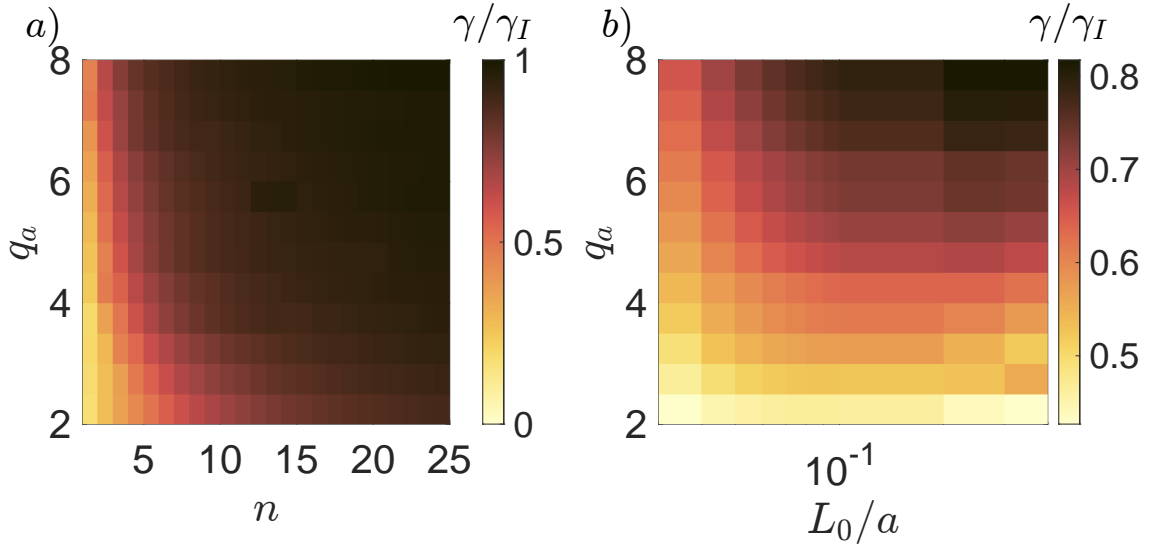


FIG. 8. Largest growth rate as a function of safety factor at the edge q_a and of the mode number n in (a) and as a function of q_a and L_0 in (b). In a), $L_0 = 0.2a$, while

in b) n is fixed to 4. In both cases, $q_0 = 2$.

V. GLOBAL LINEAR STRUCTURE OF THE BALLOONING MODE

Figure 7 shows the resulting eigenmodes poloidal structure for the modes dominating the non-linear simulation, $n = 3$ and $n = 1$ (as seen from Fig. 5), for the high- and low-shear cases, respectively. In the high shear case, the values of q_0 and q_a are such that \hat{q} and \hat{s} at $a/2$ are close to the corresponding ones

at the edge in the nonlinear simulations. The low-shear eigenmode is highly coherent, with a dominant $m = 2$ mode with no clear localisation around $\theta = 0$. On the other hand, the high-shear eigenmode reveals a filamentary structure localised on the low-field side with high poloidal modes coexisting with a dominant $m = 8$ mode. In both cases, the dominant poloidal mode number is consistent with the non-linear simulation results. In addition, the mode is radially localised around the

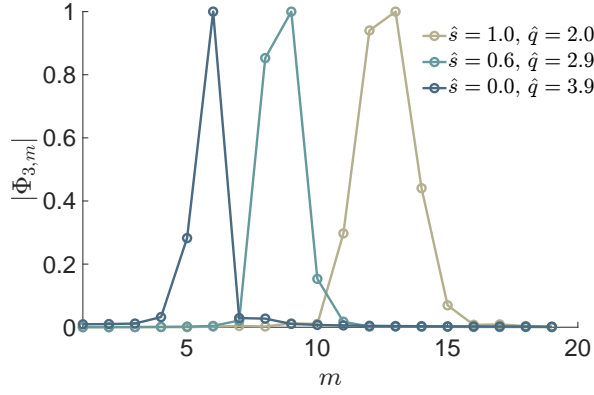


FIG. 9. Poloidal spectrum of the eigenmode at \hat{r} for $n = 3$ and different \hat{s} . Each curve is normalised so that its maximum is at 1.

peak of the equilibrium gradient, and the eigenvalue of the fastest growing mode is real, consistently with previous studies on resistive ballooning instability in the tokamak edge that points to a purely growing mode^{10,11} for both the high- and low-shear cases. The mode structure changes, from $k_y \lesssim k_x$ in the low-shear to $k_x \ll k_y$ in the high-shear case. We note that, the influence of the shear on the radial elongation and poloidal mode structure has also been observed in linear ideal and resistive infernal modes characterising hybrid tokamak scenarios^{47,48}. Large-scale modes in low-shear configurations are also observed in linear MHD studies of the MST tokamak at $\beta \sim 5 \times 10^{-3}$, pointing to resistive wall tearing modes⁴⁹.

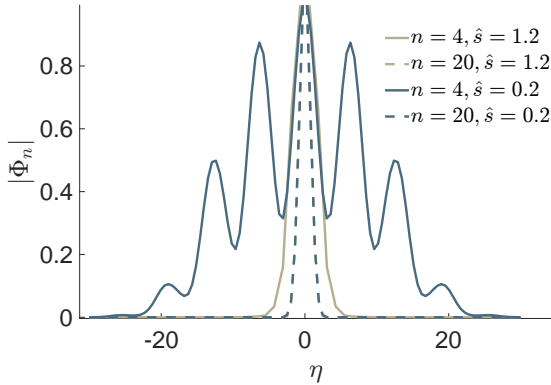


FIG. 10. Structure of the eigenmode along the ballooning angle η for different n and \hat{s} . Each curve is normalised so that its maximum is at 1.

The numerical solution shows that the most unstable mode is destabilised by increasing values of q_a , n and by the steepening of the equilibrium profile measured by L_0/a . This effect is discussed in Figure 8, where the growth rate γ is shown as a function of n (Fig. 8a) and of L_0/a in (Fig. 8b). The growth rate is normalised to the interchange growth rate, $\gamma_I = \sqrt{2R_0/L_0}^{20}$, valid in the $k_y \rightarrow \infty$ limit. We observe that, indeed, $\gamma \rightarrow \gamma_I$ in the limit of high n and q_a . We also observe that γ increases with larger resistivity and $1/L_0$, consistently with previous studies²⁰.

We investigate the poloidal mode structure by Fourier trans-

forming the poloidal profile of $|\Phi|$ and obtaining the set poloidal mode amplitudes $|\Phi_m(r)|$. We observe that the q -profile determines the dominant poloidal mode number according to the relation $m \simeq nq$, underlying the field-aligned character of the ballooning instability. In the low-shear case, m is constant along the radial direction, providing a coherent mode. On the other hand, in the high-shear case, m varies radially, resulting into a filamentary shape with a broader poloidal spectra. In this case, the poloidal mode amplitude peaks at the rational surface closest to \hat{r} . This difference between the poloidal spectrum of the high- and low-shear cases is depicted in Fig. 9, where $|\Phi_m(\hat{r})|$, is plotted for different shear values.

Increasing values of magnetic shear \hat{s} and toroidal mode number enhance the poloidal mode localisation at the low-field side, analogous to the behavior of ideal BMs in MHD³⁹. This effect is illustrated in Fig. 10 showing the magnitude of the eigenmodes plotted as a function of the ballooning angle η at the radial location \hat{r} , corresponding to the peak of the equilibrium gradient \hat{r} . In addition, modes with larger toroidal numbers n are more poloidally and radially localised, as it is shown in Fig. 11, where increasing n from 2 to 20 results in greater poloidal and radial localization of the eigenmode for two different values of \hat{s} . The ballooning character of the eigenmode is enhanced by larger values of v_0 , leading to a reduction in k_x , causing the mode structure to extend radially, as seen on the top of Fig. 12. On the other hand, more interchange-like modes are recovered by increasing ρ_*^{-1} as showed at the bottom of Fig. 12, where we perform a scan in ρ_*^{-1} keeping fixed $a/\rho_*^{-1} = 0.1$. This feature highlights the curvature-driven character of the mode, since curvature scales with $1/R_0$, which corresponds to ρ_*^{-1} in normalised units.

Consistently with previous studies²⁰, we compute the mode poloidal wavenumber as $k_y = mq(\hat{r})/\hat{r}$. On the other hand, k_x is evaluated by fitting the radial profile $|\Phi_n|$ with a Gaussian, $e^{-(r-\mu)^2/2\chi^2}$, at the low-field side, and finally defining $k_x = 1/\chi$ with μ being the Gaussian peak position. Fig. 13 indeed shows the resulting ratio, k_x/k_y , as a function of n and q_a having fixed $q_0 = 2$ (Fig. 13a), and as a function of L_0/a and q_a having fixed $q_0 = 2$ (Fig. 13b). Fig. 13 shows that the estimate $k_x \ll k_y$ is found valid for sufficiently high values of magnetic shear (high values of q_a) and toroidal mode number, as well as for large values of L_0/a . On the other hand, in the low-shear case, $k_x > k_y$, up to $n \lesssim 5$.

VI. ANALYTICAL STUDY OF THE BALLOONING MODE STRUCTURE

In this section, we provide an analytical description for the linear BM underlying the key mechanism responsible for the dependence of the mode structure on magnetic shear. To provide a unified description that is valid for all values of shear, we consider the system in Eqs. (29-31), which does not impose any functional form on \hat{f} . Reducing the problem to one equation for the electrostatic potential, decomposing in poloidal modes $\Phi = \sum_m \phi_m(r)e^{im\theta}$, and projecting on a spe-

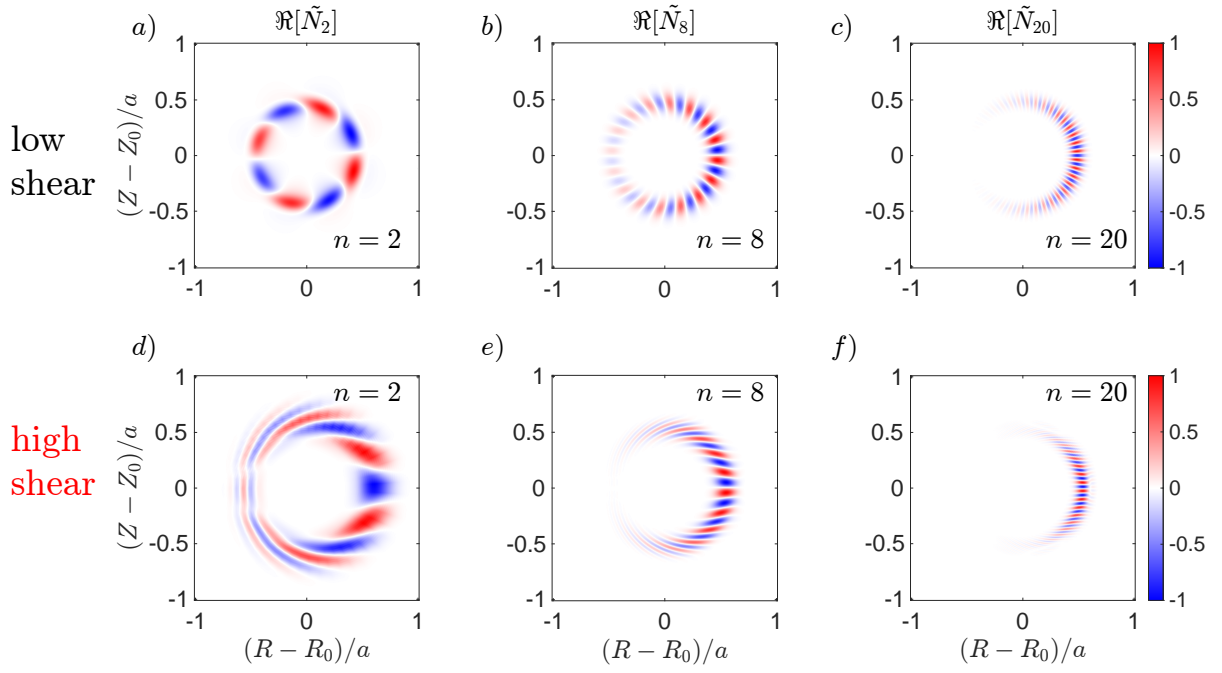


FIG. 11. Real part of the eigenmode for low shear in (a), (b) and (c) with $\hat{s} = 0, \hat{q} = 2.0$, and high shear in (d), (e), and (f) with $\hat{s} = 1.6, \hat{q} = 2.0$. The toroidal mode numbers considered are $n = 2, 8, 20$, respectively from left to right.

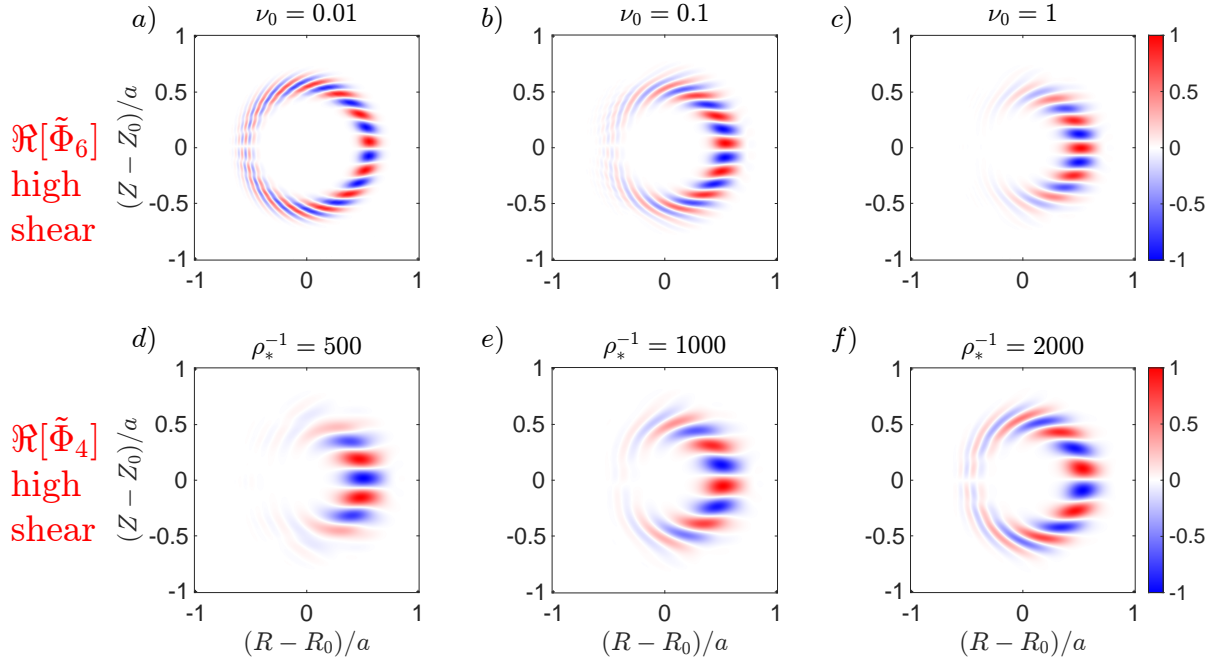


FIG. 12. On the top, $\Re[\tilde{\Phi}_6]$ for increasing values of ν_0 in a high-shear configuration with $\rho_*^{-1} = 1000$. On the bottom, $\Re[\tilde{\Phi}_4]$ for increasing values of ρ_*^{-1} , while keeping $\rho_*^{-1}/a = 0.1$ in the high shear case with $\nu = 0.1$. In both scans, $q_0 = 1.0$, and $q_a = 4.0$.

cific mode m , we obtain

$$\sigma^2 \left(\phi_m'' + \frac{\phi_m'}{r} \right) + F_{m-1} \phi_{m-1}' - F_{m+1} \phi_{m+1}' + G_m^- \phi_{m-1} - G_m^+ \phi_{m+1} - K_m \phi_m = 0, \quad (42)$$

with

$$F_m = 2\rho_*^{-1} \frac{m}{r} f_0', \quad K_m = \frac{m_i}{m_e} \frac{\sigma}{\sigma + \frac{m_i}{m_e} \frac{\nu_0}{\sqrt{f_0}}} \left(\frac{m}{q} - n \right)^2 + \frac{\sigma^2 m^2}{r^2} \quad (43)$$

$$G_m^- = 2\rho_*^{-1} \frac{m-1}{r} \left[f_0'' - \frac{m}{r} f_0' \right], \quad G_m^+ = 2\rho_*^{-1} \frac{l+1}{r} \left[f_0'' + \frac{m}{r} f_0' \right], \quad (44)$$

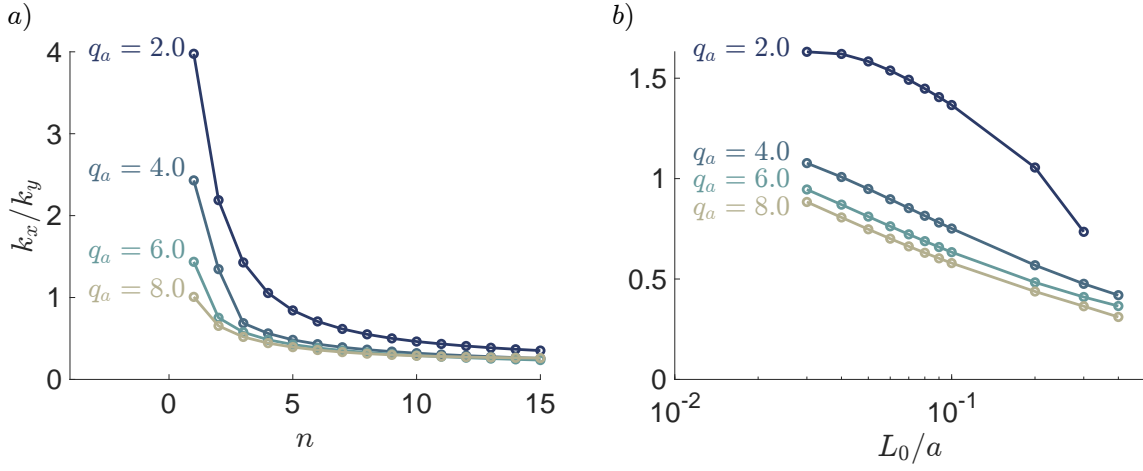


FIG. 13. In (a), k_x/k_y as a function of n for increasing q_a from 2 to 8 with $L_0 = 0.2a$. In (b), k_x/k_y as a function of L_0/a with q_a from 2 to 8 with $n = 4$. In both cases $q_0 = 2$.

for any integer m . Eq. (42) describes the coupling of a poloidal mode ϕ_m with neighbouring modes, $\phi_{m\pm 1}$. This feature, defined as poloidal mode coupling, is typical of curvature-driven instabilities in tokamaks and stellarators⁵⁰.

To progress analytically, we simplify Eq. (42) by considering that only the dominant mode $m_0 = nq(\hat{r}_q)/\hat{r}_q$, with r_q being the closest rational surface to \hat{r} , and its sidebands $m_0 \pm 1$, have finite amplitude. From Eq. (42), we have the closure relation for $\phi_{m_0\pm 1}$:

$$\phi_{m_0+1} = \frac{F_{m_0}\phi'_{m_0} + G_{m_0+1}^-\phi_{m_0}}{K_{m_0+1}}, \quad (45)$$

$$\phi_{m_0-1} = -\frac{F_{m_0}\phi'_{m_0} + G_{m_0-1}^+\phi_{m_0}}{K_{m_0-1}}. \quad (46)$$

We remark that the approach of considering the contribution from the side-bands has been used in other contexts, such as for ideal infernal modes in MHD^{48,51}.

Eqs. (45) and (46) show that mode coupling is induced by curvature effects via G_m^\pm and F_m , and damped by finite k_\parallel contributions via K_m . In the low-shear case, $\phi_{m_0\pm 1}$ are strongly damped by k_\parallel effects since the term $(m \pm 1)/q - n$ in $K_{m\pm 1}$ does not vanish anywhere in r , resulting in a coherent mode similar to the low-shear case in Fig. 7. However, curvature-induced mode coupling prevails over $K_{m_0\pm 1}$ in the high-shear case because $m \pm 1/n - q$ can vanish at some radial location close to \hat{r} , producing an enveloped poloidal mode structure, similar to the high-shear case in Fig. 7.

Eqs. (45) and (46), reveal the effect of physical parameters, such as L_0/a , v_0 , m_i/m_e , and ρ_*^{-1}/a , on the poloidal mode structure and relate them to the numerical results presented in Section V. As it can be seen from the definition of K_m in Eq. (43), resistivity and finite mass-ratio effects induce a larger mode coupling and localise the mode on the low-field side. A similar effect is obtained by increasing a/L_0 , since G_l^- and G_l^+ are proportional to equilibrium gradients. Mode coupling

is enhanced also by larger n and q since in Eqs. (45) and (46) the numerator scales with k_y and the denominator with $1/q$. Finally, at constant aspect ratio R_0/a fixed, the side-band modes $\phi_{m_0\pm 1}$ are proportional to $1/a$, meaning that larger size is related to less mode coupling.

Following previous works^{1,19}, we reduce the Eq. (42) to a Schrödinger equation for the harmonic oscillator to obtain a dispersion relation for σ . First, as detailed in Appendix B, substituting $\phi_{m_0\pm 1}$ in Eq. (42) for m_0 , and Taylor expanding around \hat{r} , we get

$$a_0\phi''_{m_0} + (b_0 + b_1x)\phi'_{m_0} + (c_0 + c_1x + c_2x^2)\phi_{m_0} = 0, \quad (47)$$

where $x = r - \hat{r}$, a_0, b_0, b_1, c_0, c_1 , and c_2 are constant complex coefficients. Taking as ansatz,

$$\phi_{m_0} = u(x)e^{-\alpha x - \frac{\chi}{2}x^2}, \quad (48)$$

$$\alpha = \frac{1}{2a_0b_0} + \frac{\sqrt{b_1^2 - 4a_0c_2}(\sqrt{a_0}b_0b_1 - 2a_0^{3/2}c_1)}{2(\sqrt{a_0}(b_1^2 - 4a_0c_2))^{3/4}}, \quad (49)$$

$$\chi = \frac{b_1}{2a_0} + \frac{1}{2}\sqrt{\frac{b_1^2 - 4a_0c_2}{a_0^2}}, \quad (50)$$

and applying the coordinate transformation,

$$\xi = \frac{b_0b_1 - 2a_0c_1}{\sqrt{2}\sqrt{a_0}(b_1^2 - 4a_0c_2)^{3/4}} + \frac{1}{\sqrt{2}}\left(\frac{b_1^2 - 4a_0c_2}{a_0^2}\right)^{1/4}x, \quad (51)$$

we obtain the Hermite equation for u : $\phi(\xi) = u(\xi)e^{-\frac{\xi^2}{2}}$, and $u'' - 2\xi u' = -2\lambda u$, with

$$\lambda = \frac{1}{2(b_1^2 - 4a_0c_2)^{3/2}} \left[-b_1^3 + 2b_1^2c_0 - 2b_0b_1c_1 + 2a_0c_1^2 + 2b_0^2c_2 + 4a_0b_1c_2 - 8a_0c_0c_2 + \sqrt{b_1^2 - 4a_0c_2}(4a_0c_2 - b_1^2) \right]. \quad (52)$$

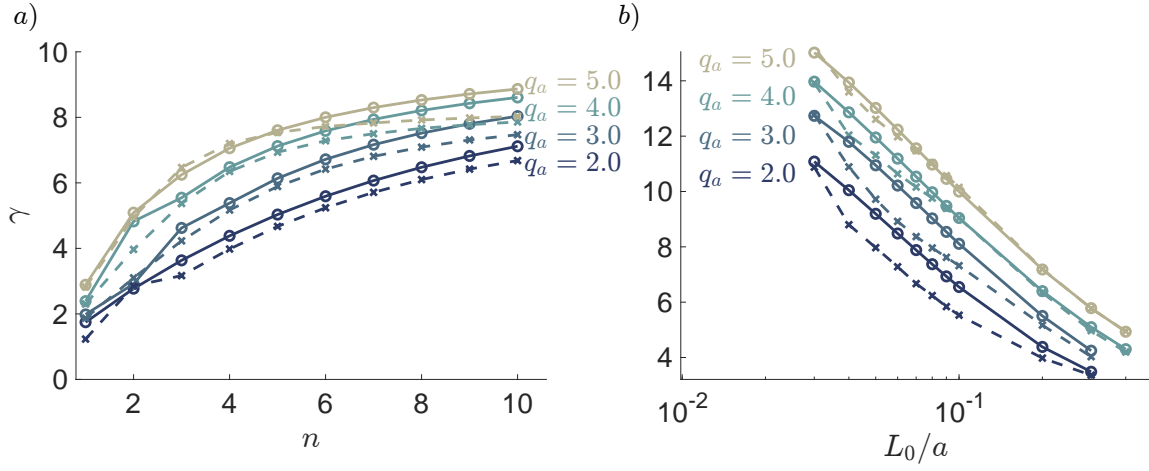


FIG. 14. In (a), γ in function of n with $L_0 = 0.2a$. In (b), γ as a function of L_0/a fixing $n = 4$. In both plots, the value of q_a is varied, while $q_0 = 2$ is fixed. The full lines are computed with the eigensolver, and the dashed lines only consider the coupling of the closest side bands.

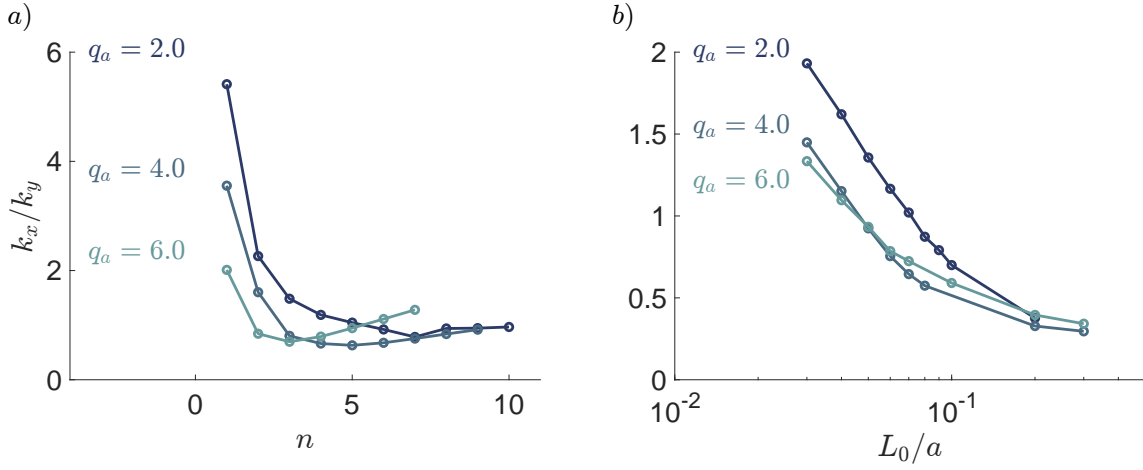


FIG. 15. In (a), k_x/k_y in function of n . In (b), k_x/k_y as a function of L_0/a with $n = 4$. In both plots, the value of q_a is varied from 2 to 8, and $q_0 = 2$ is fixed. Computations are carried out with the side-band theory.

The quantisation condition $\lambda = \delta \in \mathbb{N}$ provides the dispersion relation.

We solve numerically Eq. 52 for σ using a Newton method, considering the solution $|\phi(\xi)| \rightarrow 0$ for $\xi \rightarrow \infty$ with eigenvalue with largest growth rate. In agreement with results in Section V, it is found that the eigenvalue of the fastest growing mode is real. Moreover, the growth rate is maximised for $\delta = 0$, corresponding to an eigenmode with a Gaussian radial profile, consistent with the shape of radial profiles previously assumed in literature¹.

The comparison of the growth rates computed with the side-band theory and with the numerical ones obtained with the eigensolver in Section V is shown in Figure 14. A good overall agreement is obtained for varying toroidal mode number, q profile, and equilibrium gradient. Only a small discrepancy between the side-band theory and the numerical eigensolver is observed for increasing values of n and q_a . This effect is associated to non-vanishing high side-bands with $m = m_0 \pm 2, m_0 \pm 3 \dots$, making the approximation in Eqs. (45)

and (46) invalid.

The side-band theory allows us to reconstruct the radial and poloidal mode structure. Computing $\phi_{m_0 \pm 1}$ with Eqs. (45-46) from ϕ_{m_0} , the eigenmode is given as $\Phi(r, \theta) = \phi_{m_0+1}(r)e^{i(m_0+1)\theta} + \phi_{m_0}(r)e^{im_0\theta} + \phi_{m_0-1}(r)e^{i(m_0-1)\theta}$. Similarly to the results in Section V, $k_x \ll k_y$ for large values of shear, n , and L_0 , as shown in Figure 15, and $k_y \lesssim k_x$ in the opposite regime. We observe that for large n , q_a , and L_0 values, the eigenmodes becomes strongly localised radially around \hat{r} , overestimating k_x with respect to the results in Section V. While k_y is correctly estimated, a more precise computation of k_x would require a larger number of side-band modes.

In conclusion, the local side-band theory provides a valid alternative to the numerical eigensolver for computing γ and for studying the mode structure, by simplifying the eigenvalue problem in Eqs. (29-31) to the computation of the zeros of an analytical dispersion relation. While this theory correctly reconstructs the low shear poloidal structure (see Figure 7 a), in

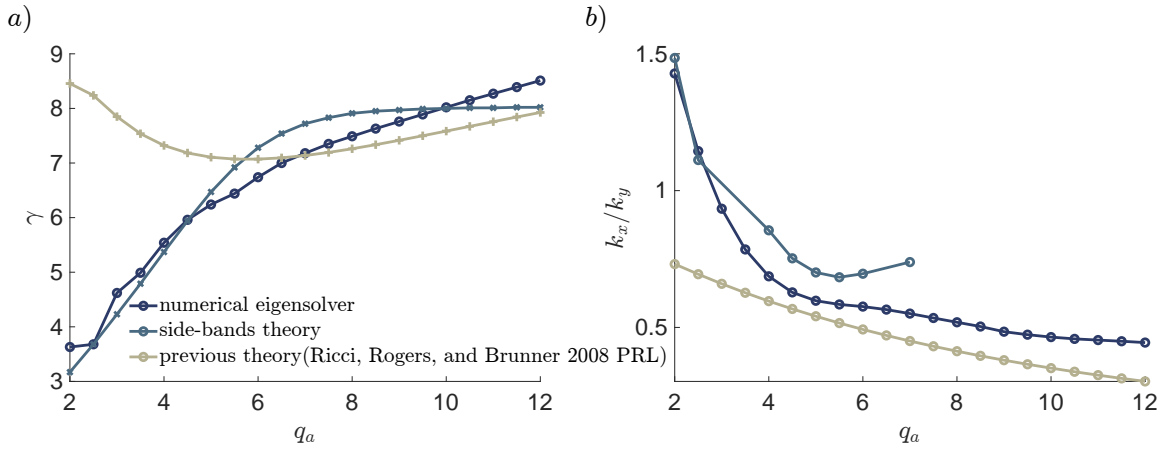


FIG. 16. In a), comparison between the resulting γ from the numerical eigensolver, the side-band theory, and from the theory used in Ricci, Rogers, and Brunner¹ with increasing q_a fixing $q_0 = 2$ and $n = 3$ with $L_0 = 0.2a$. In b), a similar comparison for k_x/k_y .

the high shear case (see Figure 7 d), the poloidal mode structure is poorly reproduced given the assumption of considering just three main modes.

VII. DISCUSSION AND CONCLUSION

This work investigates the effects of magnetic shear on ballooning-driven edge turbulence, focusing on its mode structure. Our investigation is motivated by the use of the assumption of fluctuation scale separation $1/L_p \ll k_x \ll k_y$ in determining nonlinear properties of edge plasma turbulence¹⁵, while recent global turbulent stellarator simulations show $k_x \sim k_y$ ².

Nonlinear simulations with an idealized circular-flux surface magnetic field reveal that BM turbulence is strongly affected by the magnetic shear. At low-shear, radial and poloidal eddy sizes are comparable in magnitude, $k_x \sim k_y$, and their associated spatial scale is comparable to L_p , with coherent modes dominating the dynamics. In contrast, high-shear simulations recover the $k_x \ll k_y$ condition, with broad-band turbulent spectra generated by strong interaction between poloidal modes, identified as mode coupling. In both cases, turbulence shows field-aligned turbulent structures, as expected from BM turbulence.

To understand the effect of magnetic shear, we introduce a global two-dimensional linear theory for ballooning instabilities, valid at low- and high-magnetic shear, (29-31). Using the ballooning representation, Eqs. (35-37), we compute solutions for non-vanishing shear cases. Instead, a single-mode representation is employed for vanishing-shear cases, where the ballooning representation becomes inconsistent, Eqs. (39-41).

Numerical results from the linear theory qualitatively explain the mode structures observed in nonlinear simulations, showing a transition from coherent modes to a filamentary structure with a broader poloidal spectra, as the value of shear increases. We find that the poloidal mode structure is charac-

terised by a high-frequency oscillating poloidal envelope with filamentary eddies and with dominant mode ϕ_m with $m \simeq nq$, thus minimizing k_{\parallel} . In the low-shear case, this relation is satisfied along the radial direction by $m = q_0 n$, where q_0 is the constant value of the q -profile, giving rise to a coherent mode with comparable radial and poloidal extensions. On the other hand, in the presence of a non-vanishing shear, the value of m that minimises k_{\parallel} depends on the radial position to maintain the field-aligned feature, giving rise to a large poloidal spectrum and providing a filamentary structure. Numerical results show that localisation on the low-field side is induced by n , δ , L_0 , and v_0 , while coherency is recovered for increasing R_0 , at constant aspect ratio. The mode radial scale is set by the radial pressure gradient length, L_0 , and increases with v_0 . Our study confirms that the property $k_x \ll k_y$ scaling emerges only at sufficiently high shear and toroidal mode numbers, while the property $k_x \sim k_y \sim 1/L_p$ emerges in the low-shear regime.

A side-band approach that models the BM by considering interactions between a dominant poloidal mode $m_0 = n\hat{q}$, where \hat{q} is the value of the q -profile at the rational surface, and its nearest neighbour allows us to investigate the physical mechanism influencing the mode structure transition with increasing shear. This approach shows that curvature induces mode coupling and broadens the poloidal spectrum, while finite k_{\parallel} effects contribute to concentrate the spectrum around m_0 . This theory efficiently computes γ , k_x , and k_y , correctly capturing the transition in mode structure between low- and high-shear. Limitations are found for large values of shear and toroidal mode numbers, corresponding to modes with large poloidal spectra, where three modes are not sufficient to completely describe the poloidal structure.

To emphasize the importance of a global linear theory, the global approaches introduced in this work are compared to the previous results in^{1,52} where the relation $k_x \sim \sqrt{k_y/L_p}$ is derived assuming that $k_y L_p \gg 1$, therefore radially studying the BM at the LFS. More details about this poloidal expansion can be found in Appendix C.

In Figure 16, we compare γ , and k_x/k_y from the numerical eigensolver, the side-band theory, and the poloidal expan-

sion approach. The latter does not recover the results from the global approaches for low-shear values, while for increasing shear values, its trend is captured. This deficiency resides in the assumption of expanding around the low field side, therefore assuming the localisation of the mode in that region. However, this assumption is incorrect in the low-shear case. On the other hand, the side-band approach allows us to correctly capture γ for both low and large shear values, and k_x/k_y from low- to intermediate-shear values. However, describing the poloidal structure of high shear mode requires a more significant number of poloidal modes. Therefore, the global feature of the linear models proposed in our work avoids the poloidal¹ and radial²⁰ localization assumptions of previous studies, providing a robust framework to describe the properties of global BM depending on the magnetic shear.

The work presented here offers valuable insights for the analysis of turbulence in the plasma boundary of fusion devices. For instance, it allows extending and improving non-linear estimates for the equilibrium pressure gradient length, the SOL width, and turbulent particle or heat fluxes^{15,16,18}. The natural extensions of the proposed global linear theory for the BM include investigating the electrostatic BM with shaping effects^{17,53}, in diverted configurations, with velocity and $E \times B$ shear effects, while incorporating electromagnetic contributions. This framework can also be extended to investigate DWs and KH instabilities. Despite the increased complexity, this approach can also be applied to study large-scale global modes recently identified in low-shear stellarator simulations^{2,21,23}.

ACKNOWLEDGEMENTS

Many useful discussions with D. Mancini, L.N. Stenger, and S. Brunner are gratefully acknowledged. The simulations presented herein were carried out in part at the Swiss National Supercomputing Centre (CSCS) under the project ID s1182, and in part using supercomputer resources provided under the EU-JA Broader Approach collaboration in the Computational Simulation Centre of International Fusion Energy Research Centre (IFERC-CSC). This work has been carried out within the framework of the EUROfusion Consortium, via the Euratom Research and Training Programme (Grant Agreement No 101052200 — EUROfusion) and funded by the Swiss State Secretariat for Education, Research and Innovation (SERI). Views and opinions expressed are however those of the author(s) only and do not necessarily reflect those of the European Union, the European Commission, or SERI. Neither the European Union nor the European Commission nor SERI can be held responsible for them. This work was supported in part by the Swiss National Science Foundation (10001273, BD). This research was also supported by a grant from the Simons Foundation (1013657, JL).

DATA AVAILABILITY STATEMENT

The data that support the findings of this study are available from the corresponding author upon reasonable request.

DECLARATION OF INTEREST

The authors report no conflict of interest.

Author contributions

Zeno Tecchioli: Conceptualization (equal); Data curation (equal); Formal analysis (lead); Investigation (equal); Methodology (lead); Software (lead); Validation (equal); Visualization (lead); Writing - original draft (lead); **Antonio Coelho:** Conceptualization (equal); Investigation (equal); Software (equal); Writing - review & editing (equal); **Joaquim Loizu:** Conceptualization (equal); Supervision (equal); Writing - review & editing (equal); **Brenno De Lucca:** Conceptualization (equal); Validation (equal); Writing - review & editing (equal); **Paolo Ricci:** Supervision (equal); Writing - review & editing (equal);

Appendix A: Numerical implementation of the linear solvers

We use a finite difference scheme to solve all the eigenvalue problems considered in the present work. In the following, we indicate with the coordinate y corresponding to the poloidal direction, θ for the solution of Eqs. (30-31) and Eqs. (39-41), or the ballooning one η for the solution of Eqs. (35-37). In the ballooning representation, $\eta \in [-\eta_M, \eta_M]$. To avoid the coordinate singularity at $r = 0$, we set as domain $x \in (\epsilon, 1]$, with $\epsilon = 0.01/a$, and $x = r/a$. We construct a 2D grid \mathbf{x}_{ij} as the set of points $\mathbf{x}_{ij} = (x_i, y_j)$ with $i \in [0, N_x]$, $j \in [0, N_y]$, $x_i = (a - \epsilon)i/N_x + \epsilon$, and $y_j = 2j/N_y - 1$. The size of \mathbf{x}_{ij} is $N_x \times N_y$. The resulting grid is equispaced in both directions with $\Delta x = 1/N_x$ and $\Delta y = 2/N_y$. We evaluate each field on the grid points and indicate them as N_{ij} , T_{ij} , V_{ij} , Φ_{ij} . These matrices are vectorised to construct the vector $\Psi = (N_{00}, \dots, N_{0j}, N_{10}, \dots, N_{1j}, \dots, N_{N_x N_y}, T_{00}, \dots, T_{N_x N_y}, V_{00}, \dots, V_{N_x N_y}, \Phi_{00}, \dots, \Phi_{N_x N_y})$. Consequently, the size of Ψ is $4 \times N_x \times N_y$. Derivatives are discretised by using a 6th order accurate finite difference scheme. The eigenvalue problems are recast into a matricial form as: $\sigma L \Psi = M \Psi$, where L and M are the discretisation of the left-hand-side and of the right-hand-side of the eigenvalue problems, respectively. For problems in Eqs. (30-31) and Eqs. (39-41), we impose periodic boundary conditions in the y direction by stating that $y_{i, N_y+1} = y_{i,0}$. Radially, we impose either homogeneous Neumann boundary conditions or homogeneous Dirichlet. No boundary condition is applied at $x = 0$ because of radial symmetry. Solving with the ballooning formalism, we set homogeneous Dirichlet at the boundary in η to enforce the localisation of the eigenmode.

The boundary conditions effectively reduce the number of free parameters, i.e. independent elements in the vector Ψ . This is typically done by imposing that a specific number of lines in the operators vanish. This procedure introduces a degeneracy since $\det M = 0$. To avoid this problem, we construct a projector operator, P , whose action transforms the physical eigenvector, η , which is constituted only by physical degrees of freedom, into the eigenvector with the particular boundary condition, $\Psi = P\eta$. P is constructed element-wise from the desired boundary conditions. Hence, the number of columns of P coincides with the physical degrees of freedom, while its number of lines accounts for the number of points in the grid. Therefore, P is a rectangular matrix, while P^{-1} is defined as the inverse of P such that $P^{-1}P = I_d$. The boundary value problem is given by $\gamma L\Psi = \gamma LP\eta = MP\eta$ whose inversion is $\gamma\eta = (P^{-1}LP)^{-1}P^{-1}MP\eta$, yielding an eigenvalue problem for the operator $(P^{-1}LP)^{-1}P^{-1}MP$, which acts in the space of physical degrees of freedom and is not degenerate. The left multiplication by P^{-1} is necessary for having $P^{-1}LP$ squared and invertible. P is a pseudo-projector since the dimensions of the two rectangular matrices do not allow the product PP . We numerically solve the eigenvalue problem by finding the set of σ and η , and we obtain the constrained eigenmode via $\Psi = P\eta$. Among the values of σ and the corresponding eigenvectors η , the one expected to dominate the dynamics and to saturate the equilibrium is associated with the fastest growing mode, i.e. the one with the largest real part of σ . In addition, M and L matrices are large-scale sparse matrices without any particular symmetry.

We solve the problem using the Arnoldi iteration^{45,54}, which considers $M^\alpha \mathbf{b}$ as the closest approximation to the eigenvector of a matrix M corresponding to the largest γ , with starting vector \mathbf{b} , and with a positive integer α . This method can be tailored for finding the eigenvalue with the largest real part. The matrices are handled with the ARPACK library⁵⁵, and the algorithm is implemented in the `eigs` function in MATLAB⁴⁶. We fix the $\alpha = 350$ with 10^{-8} as tolerance in the numerical implementation.

For each σ found, we check that it satisfies Gerschgorin's Circle Theorem⁵⁶. We then study the influence of the grid size $N_G = N_x \times N_y$ on σ by varying N_x and N_y . We consider σ converged if σ obtained with N_G grid and for σ' obtained with N'_G , with $N'_G > N_G$, are such that $|\gamma - \gamma'| < 10^{-4}$. Using the ballooning representation, we checked that the result is unaffected by increasing η_M .

Appendix B: Derivation of Eq. (47)

Substituting $\phi_{m_0 \pm 1}$ in Eq. (42) for m_0 , we obtain the boundary value problem:

$$K_2(r)\phi''_{m_0} + K_1(r)\phi'_{m_0} + K_0(r)\phi_{m_0} = 0, \quad (\text{B1})$$

where K_0 , K_1 , and K_2 expressions are

$$K_0 = \frac{F_{m_0-1}}{K_{m_0-1}^2} \left(G_{m_0-1}^+ K_{m_0-1}' - G_{m_0-1}' K_{m_0-1} \right) - \frac{G_{m_0}^- G_{m_0-1}^+}{K_{m_0-1}} - K_{m_0} - \frac{1}{K_{m_0+1}^2} \left[F_{m_0+1} G_{m_0+1}^- K_{m_0+1}' - K_{m_0+1} (G_{m_0+1}^- G_{m_0}^+ + F_{m_0+1} G_{m_0+1}') \right], \quad (\text{B2})$$

$$K_1 = -\frac{1}{K_{m_0+1}^2} \left\{ \frac{K_{m_0+1}}{r K_{m_0-1}^2} \left[K_{m_0+1} K_{m_0-1} (-K_{m_0-1} + r F_{m_0-1} (G_{m_0-1}^+ + F_{m_0}')) \right] + r F_{m_0} \left[G_{m_0}^+ K_{m_0-1}^2 + K_{m_0+1} (G_{m_0}^- K_{m_0-1} - F_{m_0-1} K_{m_0-1}') \right] + F_{m_0+1} \left[K_{m_0+1} (G_{m_0+1}^- + F_{m_0}') - F_{m_0} K_{m_0+1}' \right] \right\}, \quad (\text{B3})$$

$$K_2 = F_{m_0} \left(-\frac{F_{m_0-1}}{K_{m_0-1}} - \frac{F_{m_0+1}}{K_{m_0+1}} \right) + 1. \quad (\text{B4})$$

We expand K_0 , K_1 , and K_2 at $r = \hat{r}$ where the equilibrium gradient peaks. Defining $x = r - \hat{r}$, we find $K_0 = c_0 + c_1 x + c_2 x^2$, $K_1 = b_0 + b_1 x$, and $K_2 = a_0$, with $a_0, b_0, b_1, c_0, c_1, c_2$ depending on n, q, s and σ , obtaining Eq. (47).

Appendix C: Local poloidal theory for the BM

The system of Eqs. (29-31) can be reduced to a boundary value problem for Φ vanishing at $r = 0$ and a . Expanding the poloidal operators around $\theta = \xi = 0$ and decomposing in Fourier modes we obtain:

$$\phi_m'' + \left(\frac{1}{r} + \frac{4\rho\xi}{\sigma^2} \frac{im}{r} f_0' \right) \phi_m' + \left[-\frac{m^2}{r^2} + \frac{4\rho}{\sigma^2} \left(im\xi \left(\frac{1}{r} f_0'' - \frac{1}{r^2} f_0' \right) - \left(1 - \frac{\xi^2}{2} \right) \frac{m^2}{r^2} f_0' \right) - \frac{\frac{m_i}{m_e} \left(\frac{m}{q} - n \right)^2}{\sigma \left(\sigma + \frac{m_i}{m_e} \frac{v_0}{\sqrt{f_0}} \right)} \right] \phi_m = 0. \quad (\text{C1})$$

Since Eq. (C1) is formally equivalent to Eq. (B1), it is solved analogously by reducing it to a Schrödinger-like equation using an expansion around \hat{r} , providing a dispersion relation that we solve numerically. Given n , we then maximise γ as a function of m and similarly for ξ . We find that γ is maximised for $\xi = 0$, $m = n\hat{q}$, and $\delta = 0$ while ω is found to vanish in these cases.

¹P. Ricci, B. N. Rogers, and S. Brunner, "High- and Low-Confinement Modes in Simple Magnetized Toroidal Plasmas," *Physical Review Letters* **100**, 225002 (2008).

²A. Coelho, J. Loizu, P. Ricci, and Z. Tecchiolli, "Global fluid simulation of plasma turbulence in stellarators with the gbs code," *Nuclear Fusion* **64**, 076057 (2024).

³M. Endler, "Turbulent sol transport in stellarators and tokamaks," *Journal of nuclear materials* **266**, 84–90 (1999).

- ⁴O. Garcia, "Blob transport in the plasma edge: a review," *Plasma and Fusion Research* **4**, 019–019 (2009).
- ⁵A. Zeiler, D. Biskamp, J. Drake, and P. Guzdar, "Three-dimensional fluid simulations of tokamak edge turbulence," *Physics of Plasmas* **3**, 2951–2960 (1996).
- ⁶B. Rogers, J. Drake, and A. Zeiler, "Phase space of tokamak edge turbulence, the l-h transition, and the formation of the edge pedestal," *Physical Review Letters* **81**, 4396 (1998).
- ⁷M. Giacomini and P. Ricci, "Investigation of turbulent transport regimes in the tokamak edge by using two-fluid simulations," *Journal of Plasma Physics* **86**, 905860502 (2020).
- ⁸A. Zeiler, "Tokamak Edge Turbulence," *Max-Planck-Institut für Plasma-physik IPP* **5/88** (1999).
- ⁹P. Ricci and B. Rogers, "Turbulence phase space in simple magnetized toroidal plasmas," *Physical review letters* **104**, 145001 (2010).
- ¹⁰A. Masetto, F. Halpern, S. Jolliet, J. Loizu, and P. Ricci, "Turbulent regimes in the tokamak scrape-off layer," *Physics of Plasmas* **20**, 092308 (2013).
- ¹¹F. D. Halpern, S. Jolliet, J. Loizu, A. Masetto, and P. Ricci, "Ideal ballooning modes in the tokamak scrape-off layer," *Physics of Plasmas* **20** (2013).
- ¹²A. Loarte, B. Lipschultz, A. Kukushkin, G. Matthews, P. Stangeby, N. Asakura, G. Counsell, G. Federici, A. Kallenbach, K. Krieger, *et al.*, "Power and particle control," *Nuclear Fusion* **47**, S203 (2007).
- ¹³P. Ricci and B. Rogers, "Plasma turbulence in the scrape-off layer of tokamak devices," *Physics of Plasmas* **20**, 010702 (2013).
- ¹⁴M. Giacomini, A. Pau, P. Ricci, O. Sauter, T. Eich, A. U. Team, J. Contributors, *et al.*, "First-principles density limit scaling in tokamaks based on edge turbulent transport and implications for iter," *Physical Review Letters* **128**, 185003 (2022).
- ¹⁵M. Giacomini and P. Ricci, "Turbulent transport regimes in the tokamak boundary and operational limits," *Physics of Plasmas* **29** (2022).
- ¹⁶P. Ricci, M. Giacomini, A. Pau, O. Sauter, T. Eich, P. Manz, J. Contributors, A. U. Team, T. Team, *et al.*, "Theoretical scaling of the operational density limit in tokamaks and comparison to experimental data," in *29th IAEA Fusion Energy Conference (FEC 2023)* (2023).
- ¹⁷K. Lim, M. Giacomini, P. Ricci, A. Coelho, O. Février, D. Mancini, D. Silvagni, and L. Stenger, "Effect of triangularity on plasma turbulence and the sol-width scaling in l-mode diverted tokamak configurations," *Plasma Physics and Controlled Fusion* **65**, 085006 (2023).
- ¹⁸K. Lim, P. Ricci, L. Stenger, B. De Lucca, G. Durr-Legoupil-Nicoud, O. Février, C. Theiler, and K. Verhaegh, "Predictive power-sharing scaling law in double-null l-mode plasmas," *Nuclear Fusion* **64**, 106057 (2024).
- ¹⁹B. Rogers and W. Dorland, "Noncurvature-driven modes in a transport barrier," *Physics of Plasmas* **12**, 062511 (2005).
- ²⁰A. Masetto, F. Halpern, S. Jolliet, and P. Ricci, "Low-frequency linear-mode regimes in the tokamak scrape-off layer," *Physics of Plasmas* **19**, 112103 (2012).
- ²¹A. J. Coelho, J. Loizu, P. Ricci, and M. Giacomini, "Global fluid simulation of plasma turbulence in a stellarator with an island divertor," *Nuclear Fusion* **62**, 074004 (2022).
- ²²N. Krause, C. Lechte, J. Stöber, U. Stroth, E. Ascasibar, J. Alonso, and S. Niedner, "The torsatron tj-k, an experiment for the investigation of turbulence in a toroidal low-temperature plasma," *Review of scientific instruments* **73**, 3474–3481 (2002).
- ²³A. J. Coelho, J. Loizu, P. Ricci, M. Ramisch, A. Köhn-Seemann, G. Birkenmeier, and K. Rahbarnia, "Validation of GBS plasma turbulence simulation of the TJ-K stellarator," *Plasma Physics and Controlled Fusion* **65**, 085018 (2023).
- ²⁴A. Coelho, J. Loizu, P. Ricci, and Z. Tecchiolli, "Global fluid simulation of plasma turbulence in stellarators with the gbs code," *Nuclear Fusion* **64**, 076057 (2024).
- ²⁵D. Galassi, C. Theiler, T. Body, F. Manke, P. Micheletti, J. Omotani, M. Wiesenberger, M. Baquero-Ruiz, I. Furno, M. Giacomini, *et al.*, "Validation of edge turbulence codes in a magnetic x-point scenario in torpex," *Physics of Plasmas* **29** (2022).
- ²⁶P. Ricci, F. Halpern, S. Jolliet, J. Loizu, A. Masetto, A. Fasoli, I. Furno, and C. Theiler, "Simulation of plasma turbulence in scrape-off layer conditions: the gbs code, simulation results and code validation," *Plasma Physics and Controlled Fusion* **54**, 124047 (2012).
- ²⁷M. Giacomini, P. Ricci, A. Corrado, G. Fourestey, D. Galassi, E. Lanti, D. Mancini, N. Richart, L. N. Stenger, and N. Varini, "The gbs code for the self-consistent simulation of plasma turbulence and kinetic neutral dynamics in the tokamak boundary," *Journal of Computational Physics* **463**, 111294 (2022).
- ²⁸F. D. Halpern, P. Ricci, S. Jolliet, J. Loizu, J. Morales, A. Masetto, F. Musil, F. Riva, T.-M. Tran, and C. Wersal, "The gbs code for tokamak scrape-off layer simulations," *Journal of Computational Physics* **315**, 388–408 (2016).
- ²⁹J. Loizu, P. Ricci, F. D. Halpern, and S. Jolliet, "Boundary conditions for plasma fluid models at the magnetic presheath entrance," *Physics of Plasmas* **19**, 122307 (2012).
- ³⁰A. Masetto, F. D. Halpern, S. Jolliet, J. Loizu, and P. Ricci, "Finite ion-temperature effects on scrape-off layer turbulence," *Physics of Plasmas* **22**, 012308 (2015).
- ³¹X. Lapillonne, S. Brunner, T. Dannert, S. Jolliet, A. Marinoni, L. Villard, T. Görler, F. Jenko, and F. Merz, "Clarifications to the limitations of the s- α equilibrium model for gyrokinetic computations of turbulence," *Physics of Plasmas* **16** (2009).
- ³²F. Piras, S. Coda, B. Duval, B. Labit, J. Marki, S. Y. Medvedev, J.-M. Moret, A. Pitzschke, O. Sauter, and T. Team, "“snowflake” h mode in a tokamak plasma," *Physical review letters* **105**, 155003 (2010).
- ³³D. Oliveira, T. Body, D. Galassi, C. Theiler, E. Laribi, P. Tamain, A. Stegmeir, M. Giacomini, W. Zholobenko, P. Ricci, *et al.*, "Validation of edge turbulence codes against the tcv-x21 diverted l-mode reference case," *Nuclear Fusion* **62**, 096001 (2022).
- ³⁴H. Reimerdes, M. Agostini, E. Alessi, S. Alberti, Y. Andrebe, H. Arnichand, J. Balbin, F. Bagnato, M. Baquero-Ruiz, M. Bernert, *et al.*, "Overview of the tcv tokamak experimental programme," *Nuclear Fusion* **62**, 042018 (2022).
- ³⁵S. Munaretto, B. Chapman, B. Cornille, A. Dubois, K. McCollam, C. Sovinec, A. Almagri, and J. Goetz, "Generation and suppression of runaway electrons in mst tokamak plasmas," *Nuclear Fusion* **60**, 046024 (2020).
- ³⁶N. Hurst, B. Chapman, A. Almagri, B. Cornille, S. Kubala, K. McCollam, J. Sarff, C. Sovinec, J. Anderson, D. Den Hartog, *et al.*, "Self-organized magnetic equilibria in tokamak plasmas with very low edge safety factor," *Physics of Plasmas* **29** (2022).
- ³⁷N. Hurst, B. Chapman, J. Sarff, A. Almagri, K. McCollam, D. Den Hartog, J. Flahavan, and C. Forest, "Tokamak plasmas with density up to 10 times the greenwald limit," *Physical Review Letters* **133**, 055101 (2024).
- ³⁸B. Schmall, N. Hurst, A. Keyhani, and J. Sarff, "Characterization and stability of helical density snake structures in madison symmetric torus tokamak plasmas," *Journal of Plasma Physics* **91**, E72 (2025).
- ³⁹J. Connor, R. Hastie, and J. Taylor, "Shear, periodicity, and plasma ballooning modes," *Physical Review Letters* **40**, 396 (1978).
- ⁴⁰J. Connor and R. Hastie, "The stability of ideal magnetohydrodynamic ballooning modes in plasmas with internal transport barriers," *Physics of Plasmas* **11**, 1520–1536 (2004).
- ⁴¹J. W. Connor, R. Hastie, and J. B. Taylor, "High mode number stability of an axisymmetric toroidal plasma," *Proceedings of the Royal Society of London. A. Mathematical and Physical Sciences* **365**, 1–17 (1979).
- ⁴²J. Taylor and S. Newton, "Special topics in plasma confinement," *Journal of Plasma Physics* **81**, 205810501 (2015).
- ⁴³R. Dewar, J. Manickam, R. Grimm, and M. Chance, "n-dependence of ballooning instabilities," *Nuclear Fusion* **21**, 493 (1981).
- ⁴⁴R. Hastie and J. Taylor, "Validity of ballooning representation and mode number dependence of stability," *Nuclear Fusion* **21**, 187 (1981).
- ⁴⁵G. W. Stewart, "A krylov-schur algorithm for large eigenproblems," *SIAM Journal on Matrix Analysis and Applications* **23**, 601–614 (2002).
- ⁴⁶MATLAB, *24.1.0.2568132 (R2024a)* (The MathWorks Inc., Natick, Massachusetts, 2024).
- ⁴⁷J. Graves, M. Coste-Sarguet, and I. Krebs, "Non-linear saturation of non-resonant ideal long wavelength instabilities and application to sustained hybrid operational regimes," in *APS Division of Plasma Physics Meeting Abstracts*, Vol. 2023 (2023) pp. PP11–048.
- ⁴⁸M. Coste-Sarguet and J. Graves, "Fundamental properties of ideal and resistive infernal modes in tokamaks," *Plasma Physics and Controlled Fusion* **66**, 095004 (2024).
- ⁴⁹H. R. Strauss, B. Chapman, and N. Hurst, "Mst resistive wall tearing mode simulations," *Plasma Physics and Controlled Fusion* **65**, 084002 (2023).
- ⁵⁰J. P. Freidberg, *ideal MHD* (Cambridge University Press, 2014).
- ⁵¹L. Charlton, R. Hastie, and T. Hender, "Resistive infernal modes," *Phys Fluids B;(United States)* **1** (1989).

- ⁵²B. Rogers and W. Dorland, “Noncurvature-driven modes in a transport barrier,” *Physics of Plasmas* **12** (2005).
- ⁵³F. Riva, E. Lanti, S. Joliet, and P. Ricci, “Plasma shaping effects on tokamak scrape-off layer turbulence,” *Plasma Physics and Controlled Fusion* **59**, 035001 (2017).
- ⁵⁴R. B. Lehoucq, *Analysis and implementation of an implicitly restarted Arnoldi iteration* (Rice University, 1995).
- ⁵⁵R. B. Lehoucq, D. C. Sorensen, and C. Yang, *ARPACK users’ guide: solution of large-scale eigenvalue problems with implicitly restarted Arnoldi methods* (SIAM, 1998).
- ⁵⁶E. W. Weisstein, “Gershgorin circle theorem,” <https://mathworld.wolfram.com/> (2003).